

5-1-2014

Time Correlated Measurements Using Plastic Scintillators with Neutron-Photon Pulse Shape Discrimination

Norman Edison Richardson
University of Nevada, Las Vegas

Follow this and additional works at: <https://digitalscholarship.unlv.edu/thesesdissertations>

 Part of the [Nuclear Commons](#), [Nuclear Engineering Commons](#), and the [Remote Sensing Commons](#)

Repository Citation

Richardson, Norman Edison, "Time Correlated Measurements Using Plastic Scintillators with Neutron-Photon Pulse Shape Discrimination" (2014). *UNLV Theses, Dissertations, Professional Papers, and Capstones*. 2135.
<http://dx.doi.org/10.34917/5836154>

This Thesis is protected by copyright and/or related rights. It has been brought to you by Digital Scholarship@UNLV with permission from the rights-holder(s). You are free to use this Thesis in any way that is permitted by the copyright and related rights legislation that applies to your use. For other uses you need to obtain permission from the rights-holder(s) directly, unless additional rights are indicated by a Creative Commons license in the record and/or on the work itself.

This Thesis has been accepted for inclusion in UNLV Theses, Dissertations, Professional Papers, and Capstones by an authorized administrator of Digital Scholarship@UNLV. For more information, please contact digitalscholarship@unlv.edu.

TIME CORRELATED MEASUREMENTS USING PLASTIC SCINTILLATORS
WITH NEUTRON-PHOTON PULSE SHAPE DISCRIMINATION

By

Norman E. Richardson IV

Bachelor of Science in Mechanical Engineering
University of Nevada, Las Vegas
2012

A thesis submitted in partial fulfillment
of the requirements for the

Master of Science - Materials & Nuclear Engineering

Department of Mechanical Engineering
Howard R. Hughes College of Engineering
The Graduate College

University of Nevada, Las Vegas
May 2014

Copyright by Norman E. Richardson IV

All Rights Reserved



THE GRADUATE COLLEGE

We recommend the thesis prepared under our supervision by

Norman E. Richardson IV

entitled

Time Correlated Measurements using Plastic Scintillators with Neutron-Photon Pulse Shape Discrimination

is approved in partial fulfillment of the requirements for the degree of

Master of Science - Materials and Nuclear Engineering Department of Mechanical Engineering

Alexander Barzilov, Ph.D., Committee Chair

William Culbreth, Ph.D., Committee Member

Yitung Chen, Ph.D., Committee Member

Gary Cerefice, Ph.D., Graduate College Representative

Kathryn Hausbeck Korgan, Ph.D., Interim Dean of the Graduate College

May 2014

ABSTRACT

TIME CORRELATED MEASUREMENTS USING PLASTIC SCINTILLATORS

WITH NEUTRON-PHOTON PULSE SHAPE DISCRIMINATION

by

Norman E. Richardson IV

Dr. Alexander Barzilov, Examination Committee Chair
Associate Professor of Mechanical Engineering
University of Nevada, Las Vegas

Since the beginning of the nuclear age, there has been a strong demand for the development of efficient technologies for the detection of ionizing radiation. According to the United States' Department of Energy, the accurate assessment of fissile materials is essential in achieving the nonproliferation goals of enhancing safety and security of nuclear fuel cycle and nuclear energy facilities [1]. Nuclear materials can be characterized by the measurement of prompt and delayed neutrons and gamma rays emitted in spontaneous or induced fission reactions [2] and neutrons emitted in fission reactions are the distinctive signatures of nuclear materials. Today, the most widely used neutron detection technologies rely on thermal neutron capture reactions using a moderating material to cause the neutron to lose its energy prior to the detection event. This is necessary because as the fission event occurs, neutrons are emitted carrying high amounts of energy, typically on the order of mega electron volts (MeV). These energetic particles are classified as "fast" neutrons. For detecting the thermal neutrons, the Helium-3 (^3He) gas-filled counters are arguably the most widely used technology of neutron detection.

^3He counters have been the scientific standard for the nuclear engineering community for several decades, and have earned their place as a reliable technique for the detection of neutrons. However, ^3He gas-filled counters have several disadvantages. First, gas-filled counters are not rigid and are sensitive to vibrations. Secondly, gas-filled counters are prone to the count rate limitations due to the physical processes of charge multiplication and transport in the gas medium in the electric field. Lastly, ^3He gas-filled counters suffer from a supply shortage of the ^3He isotope. As it is stated in [3], this shortage is created by the new demand for Helium-3 due to the deployment of neutron detectors at the borders after the 9/11 attack to help secure the nation against smuggled nuclear and radiological material. Moreover, the production of ^3He isotope as a byproduct of security programs was drastically decreased. This isotope shortage coupled with the disadvantages of relying on a detector that requires neutron moderation before the detection of fission neutrons, poses a significant challenge in supporting the existing detection systems and the development of future technologies [4].

To address this problem, a reliable and accurate alternative technology to detect neutrons emitted in fissions must be developed. One such alternative technology that shows promise in this application is the use of scintillators based on solid state materials (plastics) which are sensitive to fast neutrons. However, plastic scintillators are also sensitive to photons. Hence, it is necessary to separate the neutron signals from the photon signals, using the pulse shape discrimination (PSD) analysis. The PSD is based on the comparison of the pulse shapes of digitized signal waveforms.

This approach allows for the measurement of fast neutrons without the necessity of their moderation. Because the fission spectrum neutrons are mainly fast, methods

employing fast neutron detection are applicable for the assay of fissile materials. In addition, the average time of scintillation of the plastic medium is much shorter than those of the gaseous counters, thus allowing scintillation detectors to be used in high count rate environments. Furthermore, the temporal information of the fast neutron detection using multiple sensors enables the time correlation analysis of the fission neutron multiplicity. The study of time correlation measurements of fast neutrons using the array of plastic scintillators is the basis of this work.

The array of four plastic scintillator detectors equipped with the digital data acquisition and analysis system was developed. The digital PSD analysis of detector signals “on-the-fly” was implemented for the array. The time coincidence measurement technique using the list mode was employed for two detectors operating on the single time scale. This was necessary as no fission source was available to be used as a fast neutron multiplicity source. The detection technology was tested using isotopic photon sources and a plutonium-beryllium neutron source. It was shown that the system can be effectively used for fast-neutron multiplicity measurements, through a “proof-of-concept” model, enabling a shorter width of the time coincidence window compared to the ^3He counters. This result opens prospects to reduce the false coincidence rates in the neutron multiplicity measurements, thus increasing the sensitivity of nuclear material detection.

ACKNOWLEDGEMENTS

First, it is important for me to acknowledge my advisor, Dr. Alexander Barzilov. I entered my Master's Degree track torn between Aerospace Engineering and Nuclear Engineering. Two months prior to graduating with my Bachelor of Science in Mechanical Engineering I received news that a new professor would be starting in the Fall of 2012 and that his focus was in Nuclear Engineering. I saw this as a sign that the University was expanding its Nuclear Engineering program, and that this new professor was the first step in that direction. After talking to Dr. Barzilov about the things he had in mind, I was astonished by the technology he was invested in and how little I knew about it. This drove me into Nuclear Engineering. My first class in the subject was taught by Dr. Barzilov, and he showed me a taste of the technology that nuclear engineering can provide, and I wanted to be involved. Dr. Barzilov motivated me to commit to the degree, and ever since that first day in his Introduction to Nuclear Engineering class, he has motivated me and supported me in my nuclear endeavors. I cannot thank Dr. Barzilov enough for opening my eyes to so many possibilities.

Another important acknowledgement goes out to Terrance Kell and to Anthony Filipiak of the University of Nevada, Las Vegas Department of Mechanical Engineering Machine Shop. Both Terrance (Terry) and Anthony (Tony) helped with the construction of the plastic scintillator detectors used in this research. These two took time out of their day to accommodate me and to get my parts back to me quickly, so that the thesis was not hindered. I can't thank these guys enough for the work they put in for me.

Next, I would like to thank Mr. Mike Momayezi and Mr. Mike Hailson at Bridgeport Instruments (BPI). BPI's equipment was important for this research and their

support allowed me to adequately educate myself on the platform. For months, I pestered these gentlemen with consistent questions, and they took time out of their schedules to assist me. If it wasn't for their continual support, none of this research would have been possible.

In addition, I would like to acknowledge my lab mates, Amber Guckes and Jessica Hartman. Amber is new to the Nuclear Engineering Program but has been relentless in her studies. She provided me with the tools necessary to complete the MCNP based calculations of this research. She wrote the input code and helped interpret the outputs. She has been a great addition to the Nuclear Engineering Program, and I know she will prove to be a great asset to its research development. Jessica started a semester after I did and has become the resident MCNP expert. Anytime that I run into a problem with my MCNP codes, Jessica has always been able to determine the error and help correct it. She has proven to be a very valuable addition to the team and a great friend.

I feel it is also important for me extend my gratitude to the men who sit on my thesis committee. First, I would like to thank Dr. Gary Cerefice for taking time out of his schedule to provide me with direction and support in my research. I chose Dr. Cerefice to represent the Graduate College of the University of Nevada, Las Vegas, because I have had a great deal of respect for him since my first class with him. Rather than just provide answers, he encourages me to think about the possible solutions. It's because of this I wanted him to be one of the members of my Thesis Defense Committee as I knew he would not let me go unchallenged. Thank you Dr. Cerefice for being a great asset in my academic development. Also, I would like to thank Dr. William Culbreth. Dr. Culbreth has always made me think about engineering, mathematics, and life in general. I have

never been so blown away by someone's intellect as I have when I am sitting in one of Dr. Culbreth's classes, and I would like to thank him for helping to teach me and to guide me on my path in nuclear engineering. Lastly, my sincere appreciation goes out to Dr. Yitung Chen. Dr. Chen is one of the professors at the College of Engineering, and he taught me a number of my undergraduate engineering courses. Each course was a nail biter, but I can proudly say that I never left any one of Dr. Chen's classes without learning something. He has always been a beacon of guidance for me, and has always taken great interest in my development. Dr. Chen is not only my professor, but also someone that I proud to call a role model and a friend.

Lastly, and most importantly, my deepest appreciation goes out to my loved ones. My family has always supported me in enhancing my education. My parents have been unwavering and have always been there to catch me when I fell. My mother, being the mother that she is, has been there to take care of me when I was sick from too many nights of "burning the midnight oil", and my father has always been there to challenge me to make myself the very best man that I can be. Without my parents, none of my accomplishments could have been attained as they have always provided me with the very best life possible. I also cannot leave out my little sister, who is now doing her undergraduate studies at the University of Nevada, Las Vegas. My sister has bent over backwards for me for seven long years, and she has always been there to support me in my academics, even reading some of my most technical papers and providing me with great, unbiased, feedback. She will far exceed me in education, and I am sure she will revel in this statement for all time.

DEDICATION

To Jenny Ting – The motivation for it all

TABLE OF CONTENTS

ABSTRACT	iii
ACKNOWLEDGEMENTS	vi
DEDICATION	ix
LIST OF TABLES	xii
LIST OF FIGURES	xiii
CHAPTER 1: INTRODUCTION	1
1.1 Background.....	1
1.2 Project Motivation	1
1.3 Project Objectives	5
1.4 Nuclear and Neutron Detection Fundamentals.....	6
1.5 Scintillator Detectors.....	29
1.6 Time Correlation Measurements	30
CHAPTER 2: LITERATURE REVIEW	32
2.1 Helium-3 Alternatives.....	33
2.2 Review of Neutron Detection with Scintillators.....	35
2.3 Review of Neutron Multiplicity Measurements	39
CHAPTER 3: EXPERIMENTAL STUDY	42
3.1 Component Descriptions and Specifications.....	42
3.2 Detector Assembly.....	52

3.3 Laboratory Environment	54
3.4 Experimental Setup	57
CHAPTER 4: RESULTS AND DISCUSSION.....	61
4.1 Neutron Measurements using Single Detector System.....	61
4.2 Time Correlation Measurements using Two Detector System.....	78
4.3 MCNP Modeling Results	87
CHAPTER 5: CONCLUSIONS AND FUTURE WORK.....	92
APPENDICES.....	96
REFERENCES.....	97
VITA.....	103

LIST OF TABLES

Table 1 - Sub-Atomic Particles	7
Table 2 - Classification of Neutrons based on their Energy [10].....	9
Table 3 - EJ-299-33 Scintillator Parameters [55].....	43
Table 4 – Inputs of eMorpho GUI [61]	64
Table 5 –Inputs of eMorpho GUI for ^{60}Co Measurements	67
Table 6 – Input Values for qMorpho System.....	79

LIST OF FIGURES

Figure 1 - ^3He Gas Filled Neutron Detector [7].....	2
Figure 2 – Carbon Atom Structure [9].....	7
Figure 3 - ^{235}U Total Cross-Section Data [11].....	10
Figure 4 - ^{210}Po Decay: Alpha-Particle Straight-Path Tracks in a Cloud Chamber [12]...13	
Figure 5 - Bragg Curve [13].....	13
Figure 6 - Stopping Power of Charged Particles in Water [14]	15
Figure 7 - Continuous Slowing Down Approximation Range for Gold, Silicon and Polystyrene [15]	17
Figure 8 - Compton Scattering: θ and ϕ are the Scattering Angles for $h\nu'$ and Electron, Respectively [16].....	19
Figure 9 - Relative Importance of Three Major Processes [17].....	20
Figure 10 - Inelastic Collision Between a Neutron and a Nucleus [18]	21
Figure 11 - Elastic Collision Between a Neutron and a Nucleus [18].....	22
Figure 12 - Fission of ^{235}U Nucleus [20]	24
Figure 13 - Products of Thermal Neutron Fission of ^{233}U , ^{235}U , and ^{239}Pu [21].....	25
Figure 14 - ^{235}U Cross-Section Data; Total Cross-Section (Green), Total Absorption Cross-Section (Blue), Elastic Cross Section (Blue) [11]	26
Figure 15 - ^3He Total Absorption Cross-Section Data [22].....	27
Figure 16 - Avalanche Development Around a Thin Wire of Gaseous Counter [12].....	28
Figure 17 – Example of Neutron Multiplicity Measurement System [23]	31
Figure 18 - EJ-299-33 Plastic Scintillating Material.....	44
Figure 19 - EJ-299-33A Plastic Scintillating Material	44

Figure 20 – EJ-299-33 (Left) and EJ-299-33A (Right) Comparison	44
Figure 21 - Design Schematic of the ADIT B51B03W PMT [56]	46
Figure 22 - Absolute Sensitivity & Quantum Efficiency of B51B03W PMT [56].....	47
Figure 23 - B51B03W PMT by ADIT.....	48
Figure 24 - eMorpho Data Acquisition Device from BPI [57]	48
Figure 25 - 4-Channel DAQ: qMorpho	50
Figure 26 - Plastic Scintillator Detector: (a) the Scintillator Enclosure, (b) the PMT Enclosure, and the (c) eMorpho Hardware	54
Figure 27 - Plutonium-Beryllium (Pu-Be) Source in the Nuclear Measurements Laboratory at UNLV	55
Figure 28 - Pu-Be Source Schematic Showing the (A) Pu-Be Source in the "Closed" Position, and the (B) Neutron Beam Port	56
Figure 29 - Single Detector Experiment with Pu-Be Source	58
Figure 30 - Decay Scheme of ^{60}Co [60]	58
Figure 31 - Time Correlated Measurement using Two Detectors and ^{60}Co Source.....	59
Figure 32 - Schematic of the Four Detector Array Setup for Multiplicity Modeling	60
Figure 33 - Calibration of Neutron Scintillator Detector.....	62
Figure 34 - ^{60}Co Source used to Calibrate EJ-299-33A Detector System.....	62
Figure 35 - eMorpho GUI.....	63
Figure 36 - Default Basic Controls Panel in the eMorpho GUI.....	64
Figure 37 –HV Setup Panel	65
Figure 38 - Pulse Shape Discrimination Scheme Showing Differences in Photon and Neutron Trace Signals [12]	66
Figure 39 – GUI Calibration of Detector using ^{60}Co Source.....	69
Figure 40 – Energy Histogram of ^{60}Co Source with a Gaussian Fit	70

Figure 41 – Energy Histogram of ^{137}Cs Source with a Gaussian Fit	71
Figure 42 – PMT Anode Pulse Produced by a Photon	73
Figure 43 – PMT Anode Pulse Produced by a Neutron	73
Figure 44 –Photon and Neutron Traces from Pu-Be Source	74
Figure 45 – PSD Analysis Results of Pu-Be Neutron/ Gamma Source	75
Figure 46 – Pu-Be PSD Distributions Based on Radiation’s PID Values	76
Figure 47 –PSD Results from ^{60}Co Showing no Grouping of Neutrons	77
Figure 48 – ^{60}Co PSD Distribution Showing Pure Photon Distribution.....	77
Figure 49 – qMorpho Time Coincidence Measurement of ^{60}Co on Two Channels.....	80
Figure 50 – Concatenated Pulses of qMorpho Measuring Two Detections of Radiation from ^{60}Co Source.....	81
Figure 51 – Time Stamp Coincidence Between Two Channels of qMorpho	82
Figure 52 – Energy Coincidence Between Two Channels of qMorpho	83
Figure 53 – Energy Spectra of ^{60}Co on Channel 0	83
Figure 54 – Energy Spectra of ^{60}Co on Channel 1	84
Figure 55 - Time Stamp Coincidence Between Two Channels of qMorpho with Coincidence Window at 4 ADC Clock Cycles	85
Figure 56 - Energy Coincidence Between Two Channels of qMorpho with Coincidence Window at 4 ADC Clock Cycles	85
Figure 57 - Time Stamp Coincidence Between Two Channels of qMorpho with Coincidence Window at 1 ADC Clock Cycles	86
Figure 58 - Energy Coincidence Between Two Channels of qMorpho with Coincidence Window at 1 ADC Clock Cycles	86
Figure 59 – Single Pulse Measurement of ^{239}Pu using Helium-3 Detectors.....	88
Figure 60 - Single Pulse Measurement of ^{239}Pu using Plastic Scintillator Detectors.....	88

Figure 61 – Double Coincidence of ^{239}Pu using Plastic Scintillator Detectors	89
Figure 62 - Triple Coincidence of ^{239}Pu using Plastic Scintillator Detectors	89
Figure 63 - Double Coincidence of ^{239}Pu using Helium-3 Detectors.....	90
Figure 64 - Triple Coincidence of ^{239}Pu using Helium-3 Detectors.....	90

CHAPTER 1

INTRODUCTION

1.1 Background

Researchers began working in the field of atomic radiation, atomic change, and nuclear fission in 1895 [5], and 40 years later, physicist James Chadwick was awarded the Nobel Prize for his discovery of the neutron in 1932 [6]. By 1942, the United States had begun experimenting in harnessing the neutron as a means to create nuclear weapons. This quick development of nuclear technology continued for the next six decades, and the technology spread worldwide. However, with the quick growth and spread of the technology, the nuclear industry's need for reliable neutron detectors has never more vital for achieving the non-proliferation goals of enhancing the safety and security of nuclear facilities worldwide. [1]

In order to achieve this goal, the accurate detection of neutrons is required. Since its discovery in 1932, scientists have been developing techniques to detect the neutron. In that time, various techniques have been implemented, however with the changing dynamics of the industry and the economic situation on the availability of specific neutron converting material, the need for an advanced, reliable neutron detection system has grown significantly.

1.2 Project Motivation

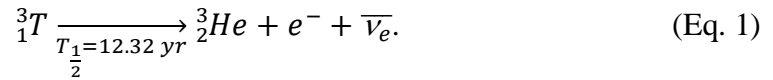
Neutron detection is accomplished by effectively placing a detector in a position within the neutron flux. Neutrons entering the detector medium interact with it generating a measurable signal that notifies the user of the presence of neutrons and provides

information on the number of detected particles and their energy in addition to the temporal and spatial characteristics of the flux. Current methods of measuring the neutron emission from fission events rely on the moderation of the fast neutrons to the low energies governed by the thermal equilibrium of neutrons with their environment. By doing this, the thermal neutron capture reactions can be utilized in neutron detection. These reactions enable conversion of neutral particles into electrically charged particles. When such interactions take place within the volume of a gaseous detector, the result is the emission of energetic charged particles which passes through the electric field creating the initial ionization cloud of electron-ion pairs. The typical proportional counter is composed of the tube filled with the ^3He gas under pressure of several atmospheres, and the thin anode wire tensioned along the tube's axis. The difference of potentials set up between the tube body and the anode sets the electric field. The motion of these charges in the electric field, with the possibility of an avalanche electron multiplication, enables measurement of the electric current induced on the detector's anode. This technique is used in the most common neutron detection methods in the world today, specifically with the use of Helium-3 (^3He) gaseous counters, such as the system shown in Figure 1.



Figure 1 - ^3He Gas Filled Neutron Detector [7]

However, this neutron detection technique has several disadvantages. First, gas-filled counters are not rigid. If a pressurized gas container breaks, then the gas would leak out and be lost to the atmosphere. Also the tensioned anode wire is prone to vibration interference, causing noise in the measured current waveforms. This poses significant problems in the field use of gaseous counters. Secondly, using gas-filled counters comes with the counting rate limitation that they have in high neutron flux conditions. Due to the physical processes of charge multiplication and transport in the gas medium in the electric field, the typical time of the anode's signal development is about one microsecond. Lastly, the important limiting factor of using detectors such as the ^3He gas counters is a lack of ^3He isotope supply. The natural abundance of Helium-3 is only about 1.4 parts per million. Rather than harvesting this isotope from the natural environment, ^3He is produced using the beta decay of tritium releasing 18.6 keV of energy following:



With the world moving in the direction of a non-proliferation era, the mass manufacturing of tritium is at a standstill, as the production of ^3He is the direct byproduct of tritium manufacturing. Thus, due to the reduction of stockpile of available ^3He and the increase in demand for thermal neutron detectors for security portals, the cost of ^3He gas has skyrocketed in recent years [3]. The combination of disadvantages of ^3He detectors with the current supply shortage problem poses a significant challenge in supporting the existing detection systems and the development of future technologies [4]. The current situation calls for the development of a reliable alternative technology to take the role that the ^3He gas-filled counters played in the detection of neutrons.

The accurate assessment of fissile materials is essential in achieving the nonproliferation goals of enhancing safety and security of nuclear fuel cycle and nuclear energy facilities in the United States and worldwide. Nuclear materials can be characterized by the measurement of prompt and delayed neutrons and gamma rays emitted in spontaneous or induced fission reactions. In addition, neutrons emitted in fission reactions are the distinctive signatures of nuclear materials. Today, the most widely used neutron detection technologies rely on thermal neutron capture reactions using a moderating material to cause the neutron to lose its energy prior to the detection event. This is necessary because as the fission event occurs, neutrons are emitted carrying high amounts of energy, typically on the order of mega electron volts (MeV). These energetic particles are thus classified as “fast” neutrons.

The fission of uranium and plutonium isotopes releases several fast neutrons simultaneously (the “neutron multiplicity event”). The average number of neutrons produced by fission, ν , is specific for the fissile isotopes of plutonium and uranium. Multiplicity technology measures the multiplicity distribution by counting fission neutrons within the coincidence resolving time (or “gate width”). The detection of neutron doublets and triplets within the gate width is the signature of the specific nuclear material. Multiplicity counting allows segregating fission reactions from the neutron background sources, such as (α, n) reactions or neutrons produced by energetic cosmic rays.

The presence of the moderator causes multiple neutron scattering events thus affecting the temporal and spatial signatures of the fission neutron emission. The gate width value is directly correlated with the false coincidence rate of measurements, and

thus the shortening of the gate width is required to decrease the false coincidence rates. A detection technology to measure fast neutrons emitted in fission events must be developed, and this approach allows for the measurement of fast neutrons without the necessity of their moderation. Because the fission spectrum neutrons are mainly fast, methods employing fast neutron detection are applicable for the assay of fissile materials. Furthermore, the temporal information of the fast neutron detection using multiple sensors enables the time correlation analysis of the fission neutron multiplicity.

These technological needs and requirements are the motivation for the project to develop an array of four fast neutron detectors equipped with the digital data acquisition and analysis system.

1.3 Project Objectives

Scintillator detectors are one such alternative technology to ^3He gas counters, and were selected for study in this project. Scintillators offer the important benefit of not having to moderate the neutron before the detection, as what is required in the ^3He detectors. Scintillators allow for the detection of neutrons in their natural fission energy spectrum (i.e. the fast spectrum). Scintillators have two primary forms: liquid and solid. Both are promising new technologies for the effective detection of fast neutrons however, the plastic scintillator has the advantage of being a solid state material, rather than a container filled with a liquid. Plastic scintillators are also easier to use with in-the-field applications. Moreover, plastics are not toxic and flammable as the majority of liquid scintillator mixtures.

The first project objective is to design and construct a neutron detector using a plastic scintillator. The second objective of this project is to develop a technique for the separation of detected gamma rays from detected neutrons, because all scintillator detectors have sensitivity to photons. Therefore, the scintillator interaction differences for neutrons and photons should be studied to allow for their effective separation. Finally, the third objective is to design an array of four scintillation detectors to study the time coincidence measurements. By accomplishing this, the system could detect multiple neutrons from the same fission reaction using the single time scale for four detector channels. This would then lead to the possibility to perform fast neutron multiplicity measurements, thus helping in achieving the non-proliferation goals.

1.4 Nuclear and Neutron Detection Fundamentals

1.4.1 Subatomic Particles

All matter is composed of particles that are common throughout, regardless of the type of matter in question. These particles, collectively referred to as sub-atomic particles, are known as protons, neutrons, and electrons. Each particle has characteristics that define the particle, and compose the quantum make up of all bodies of matter. A few characteristics of these particles are displayed in Table 1, which shows the mass (kg), of each of the subatomic particles along with its charge.

Table 1 - Sub-Atomic Particles

Sub-Atomic Particle	Mass [8]	Charge
Proton	$1.672 * 10^{-27} kg$	Positive (+)
Neutron	$1.675 * 10^{-27} kg$	Neutral
Electron	$9.109 * 10^{-31} kg$	Negative (-)

These subatomic particles make up the atom. Figure 2 shows an example of a Carbon-12 (^{12}C) atom, the most abundant isotope of carbon in the world. Every atom, as shown in the carbon atom of Figure 2, is made of a cloud of moving electrons and a densely packed center which consists of protons and neutrons. This dense center is known as the nucleus and it accounts for nearly all of the mass associated with the atom. This can be seen by comparing the individual masses for the subatomic particles using the information shown in Table 1.

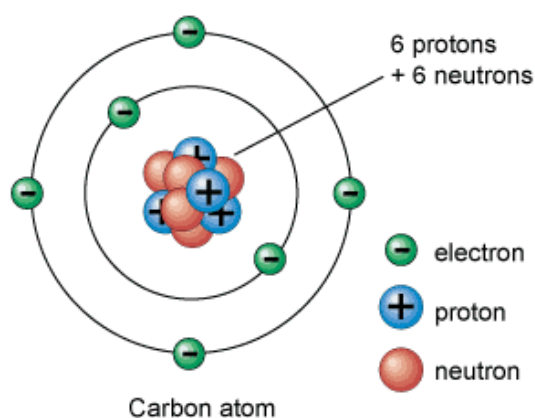


Figure 2 – Carbon Atom Structure [9]

Because of the charge differences between the proton and the electron, the two attract each other. However, the nucleus cannot be made of solely just protons due to the

similarities of their charges (i.e. positive to positive). This similarity would cause a repulsive force, thereby preventing the establishment of the structure of the nucleus. To placate the similar charges, neutrons are kept adjacent to the protons within the nucleus. As the number of protons increase, the number of neutrons that are needed to negate the repulsive forces of the protons must increase as well, such that heavy isotopes, like Uranium-235 (^{235}U), are made up of more neutrons than protons. For the case of ^{235}U , the nucleus is comprised of 92 protons and 143 neutrons.

Another subatomic “particle”, is called a photon. However, photons are not actually particles, but rather packets of electromagnetic waves. For simplicity sake, and for understanding the work for this research, it is easier to think of photons as particles. In this regard, the photon is similar to that of the neutron due to it not carrying any charge. However, photons have no mass and interact with matter differently than the neutron.

Neutrons released in nuclear reactions carry large amounts of energies, and these neutrons are thus classified in regions according to their energy levels. Table 2 shows the classifications of energetic neutrons. As neutrons gain or lose energy, they transfer into the corresponding energy classification. In most cases, thermal neutrons are the easiest to work with for neutron measurements. However, thermal neutrons are created through energy reduction techniques designed to strip the neutron of its energy through continuous interaction. When the neutron has reached thermal equilibrium, it is often much easier to absorb, and thus plays a critical role in neutron-capture based reactions.

Table 2 - Classification of Neutrons based on their Energy [10]

Neutron Energy (MeV)	Classification
$0.0 \text{ to } 0.025 * 10^{-6} \text{ MeV}$	Cold Neutrons
$0.025 * 10^{-6} \text{ MeV}$	Thermal Neutrons
$0.025 \text{ to } 0.4 * 10^{-6} \text{ MeV}$	Epithermal Neutrons
$0.4 \text{ to } 10 * 10^{-6} \text{ MeV}$	Slow Neutrons
$10 * 10^{-6} \text{ MeV to } 1 \text{ MeV}$	Resonance Neutrons
$1 \text{ MeV to } 20 \text{ MeV}$	Fast Neutrons
$> 20 \text{ MeV}$	Relativistic Neutrons

These classifications correlate to regions for matter to absorb, scatter, or fission as a result of the neutron. The probability of one of these actions taking place is known as the cross-section of the material, and carries units of barns ($1 \text{ barn} = 10^{-24} \text{ cm}^2$). An example of this data is the cross-section data shown in Figure 6, which displays the total cross-section of ^{235}U , based on data obtained by the Korean Atomic Energy Research Institute (KAERI) using the cross-section data stored in the Evaluated Nuclear Data File (ENDF) database.

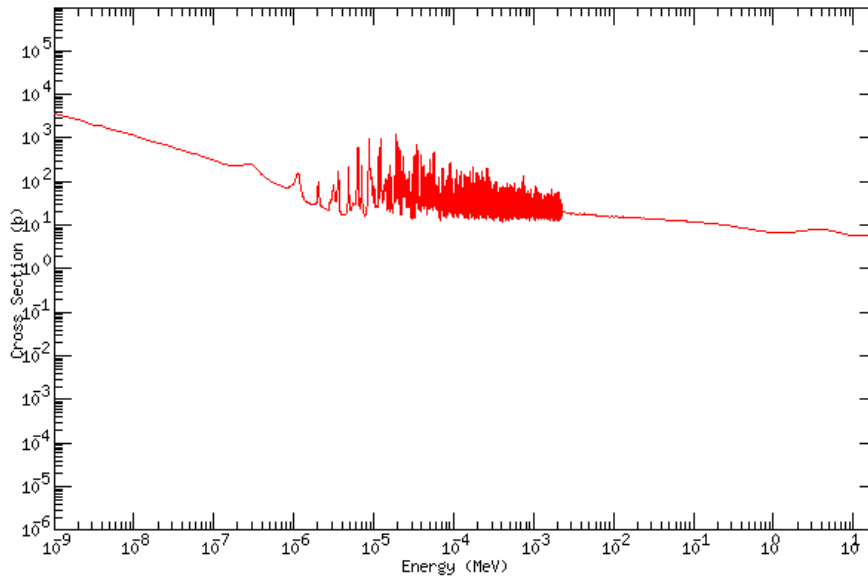


Figure 3 - ^{235}U Total Cross-Section Data [11]

1.4.2 Particle and Photon Interactions

Each of the particles (protons, electrons, alpha particles, neutrons) and photons interact with matter in a unique way.

Charged particles interact with matter via several pathways. One way is the Coulomb interaction with atomic electrons. It includes ionization (an atomic electron is ejected from the atom) and excitation (an electron goes into the excited state). Charged particles may penetrate through the atomic electron cloud and scatter from a nucleus elastically. The nucleus recoils because of energy and momentum conservation. If the charged particle is heavy and has high energy, then the recoiling nucleus may be ejected from its own electron cloud and continue to move in medium as a free charged particle. Charged particles may also undergo a nuclear reaction when it collides with a nucleus (i.e. alpha-particle induced reactions). Charged particles may also be accelerated by the

electric field of an electron cloud or a nucleus, and as a result, a photon may be emitted (the bremsstrahlung radiation). In general, passing through matter, the charge particle leaves the trail of ionization and excitation – therefore, it is called the “directly ionizing radiation”.

Non-charged particles (such as neutrons and photons) produce the charged particle in matter first; then these charged particles produce the trail of ionization and excitation passing through the matter. Therefore, they are called the “indirectly ionizing radiation”. The cross-sections for charge particle interactions are measured and tabulated in numerous nuclear databases.

It is also useful to describe how charged particles interact with matter in terms of the specific ionization – the number of ion pairs produced per unit path by a charged particle (an ion pair is an ejected electron and an ionized atom). The stopping power, S , is the total energy loss per path length by a charged particle. It is equal to the rate of decrease in energy of a particle along the path. If no nuclear reactions occur, then:

$$S = \left(\frac{dE}{dx} \right)_{col} + \left(\frac{dE}{dx} \right)_{rad} \quad (\text{Eq. 2})$$

The S is the sum of the “energy loss per unit due to collisions” (LET) and the “energy loss per unit due to radiation”. The LET is the linear energy transfer and is used to define biological effects. The LET increases with the mass and charge of a particle such that the LET of α -particles is higher than the LET of electrons (for same energy values). For example, for an energy of 1 MeV:

$$LET(\alpha) = 90 \text{ keV}/\mu\text{m} \quad (\text{Eq. 3})$$

And:

$$LET(e^-) = 0.19 \text{ keV}/\mu m \quad (\text{Eq. 4})$$

Electrons are defined as the low-LET radiation, while alpha particles are the high-LET radiation. Non-charged particles have the following LET: photons are low-LET radiation, and neutrons are the high-LET radiation.

Alpha-particles are massive and they are deflected by atomic electrons by negligible angles. Because of that, it moves in straight paths in materials. As it slows, it captures two electrons thus forming a neutral helium atom, and the specific ionization abruptly drops to zero (the “Bragg curve” shown in Figure 5). The ranges of the alpha particles (the distance where the ionization falls to zero) are measured and tabulated (e.g. in Nuclear Spectroscopy Tables). The Bragg-Kleeman rule for α -particle range in materials (using known values for air) is expressed in the following:

$$R = R_a \left(\frac{\rho_a}{\rho} \right) \sqrt{\frac{M}{M_a}} = \frac{\sqrt{M}}{\rho} R_a * (3.2 \times 10^{-4}) \quad (\text{Eq. 5})$$

In Equation 5, R is the range in a material of density, ρ , and atomic weight, M , and R_a , ρ_a , M_a are values for air. The straight-path tracks of alpha particles emitted in ^{210}Po decays in a cloud chamber are shown in Figure 4, and the typical Bragg curve is shown in Figure 5.

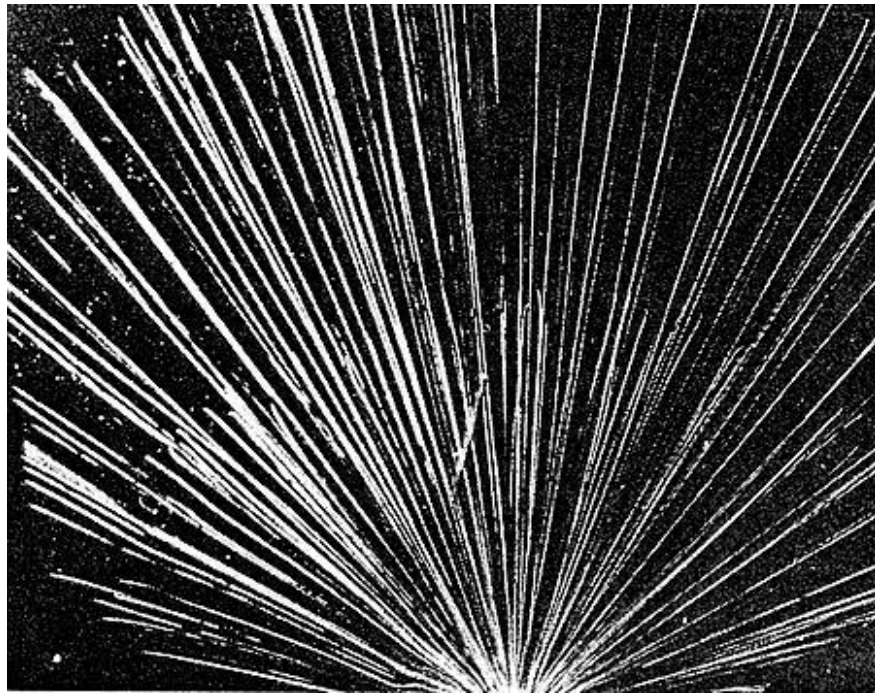


Figure 4 - ^{210}Po Decay: Alpha-Particle Straight-Path Tracks in a Cloud Chamber [12]

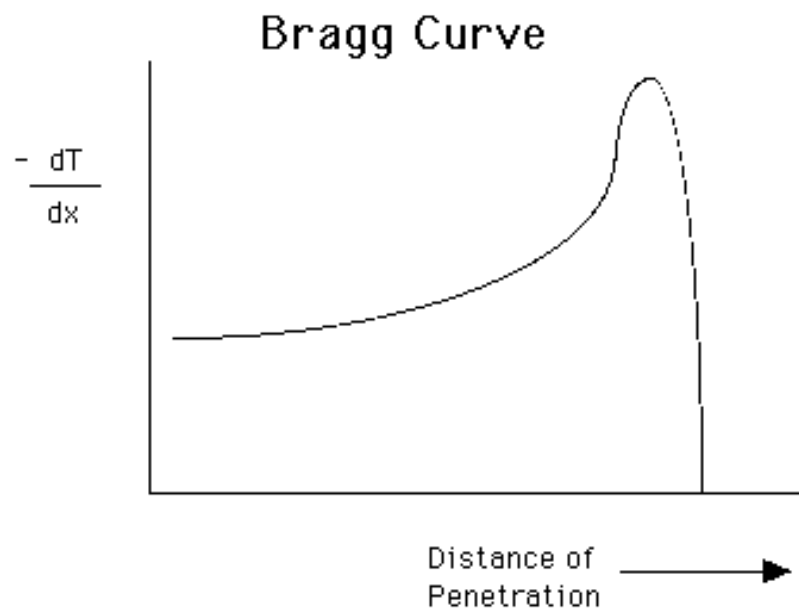


Figure 5 - Bragg Curve [13]

If the material is a mixture: then \sqrt{M} in the Bragg-Kleeman rule (Eq. 5) is replaced with:

$$\sqrt{M} = \gamma_1 \sqrt{M_1} + \gamma_2 \sqrt{M_2} + \dots + \gamma_n \sqrt{M_n} \quad (\text{Eq. 6})$$

Where γ_i are fractions of atoms having atomic weights, M_i . Relative stopping power is the ratio of the range of alpha particles in air to the range of alpha particles in the given material and it is independent of the initial energy of charged particle:

$$\frac{R_a}{R} = 3100 * \left(\frac{\rho}{\sqrt{M}}\right) \quad (\text{Eq. 7})$$

Stopping power values for most materials are high; therefore, the ranges of alpha-particles in matter are small. For example, the 5-MeV alpha-particle in aluminum has a range of just 0.0022 cm. They can even be stopped by thin layers of materials, such as a tissue or a layer of skin.

The magnitude of energy loss per unit length is the relationship between range and energy and is classified by:

$$\frac{dE}{dx} = \left(\frac{e^2}{4\pi\epsilon_0}\right)^2 \frac{4\pi z^2 N_0 Z \rho}{mc^2 \beta^2 A} \left[\ln\left(\frac{2mc^2 \beta^2}{I}\right) - \ln(1 - \beta^2) - \beta^2 \right] \quad (\text{Eq. 8})$$

Where z is the atomic number of the heavy particle, e is the magnitude of the electron charge, N_0 is Avogadro's number, m is the electron rest mass, c is the speed of light in a vacuum, β is the speed of the particle relative to c (V/c), Z is the atomic number of the stopping material, A is the atomic weight of the stopping material, ρ is the density of the stopping material, and I is the mean excitation energy of the medium. I is an

empirical constant: $I \sim 10 \cdot Z$ [eV]. For example, in air $I = 86$ eV while in aluminum $I = 163$ eV. The range is an integral over all energies of the particle:

$$R = \int_T^0 \left(-\frac{dE}{dx} \right)^{-1} dE \quad (\text{Eq. 9})$$

The stopping power of charged particles in water is shown in Figure 6.

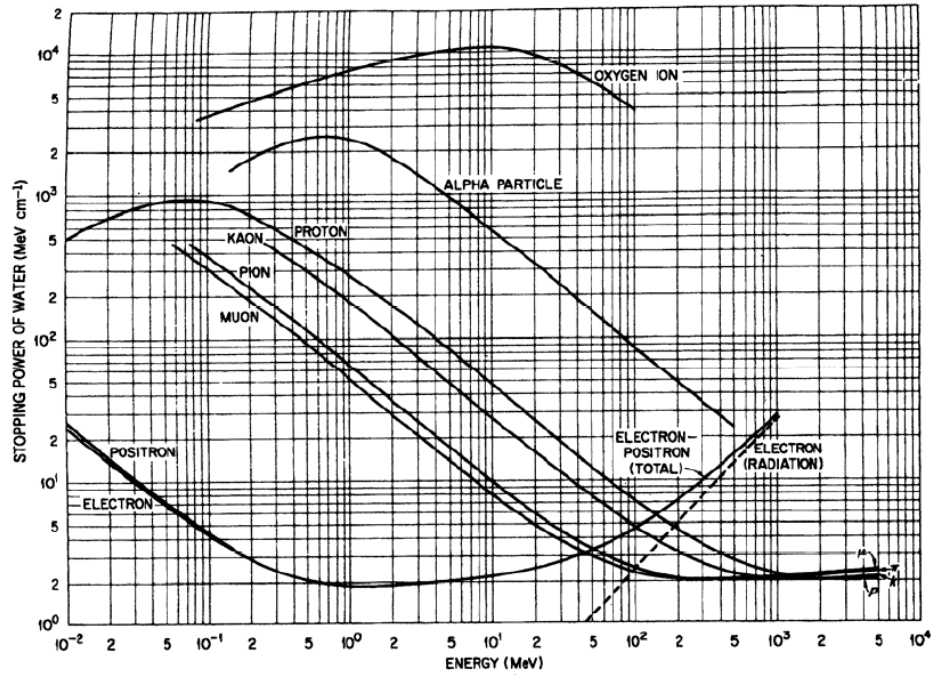


Figure 6 - Stopping Power of Charged Particles in Water [14]

Electrons interact with matter via the Coulomb scattering like heavy charged particles. Some important differences are the following: 1) Electrons have relativistic speeds (e.g., for electrons emitted in the beta decay processes), and 2) Electrons will suffer large deflections in collisions with like particles (other electrons); therefore, the range in matter will be very different. In head-on collisions of two electrons, a large fraction of initial energy may be transferred to the struck electron. Because the electron

may suffer rapid changes in the direction and magnitude of its velocity, it is subject to large accelerations. The accelerating charged particles must radiate electromagnetic energy (bremsstrahlung radiation). Thus, the expression for energy loss by the electrons must include losses due to *collisions* (col) and also *radiation* (rad):

$$\frac{dE}{dx} = \left(\frac{dE}{dx}\right)_{col} + \left(\frac{dE}{dx}\right)_{rad} \quad (\text{Eq. 10})$$

Where:

$$\left(\frac{dE}{dx}\right)_{col} = \left(\frac{e^2}{4\pi\epsilon_0}\right) \frac{2\pi N_0 Z \rho}{mc^2 \beta^2 A} \left[\ln \left(\frac{T(T + mc^2)^2 \beta^2}{2I^2 mc^2} \right) + (1 - \beta^2) - (2\sqrt{1 - \beta^2} - 1 + \beta^2) \ln(2) + \frac{1}{3} (1 - \sqrt{1 - \beta^2})^2 \right]$$

And

$$\left(\frac{dE}{dx}\right) = \left(\frac{e^2}{4\pi\epsilon_0}\right)^2 \frac{Z^2 N_0 (T + mc^2)}{137 m^2 c^4 A} \left[4 \ln \left(\frac{2(T + mc^2)}{2mc^2} \right) - \frac{4}{3} \right]$$

Where T is the kinetic energy of the electron in both equations.

This formula is valid for relativistic energies only. Below relativistic energies, the energy losses are negligible.

As an example, the continuous slowing down approximation range (CSDA), as a function of energy, is shown in Figure 7 for gold, silicon, polystyrene, and collodion. Polystyrene $(C_8H_8)_n$, has a density of 1.05 g/cm^3 and collodion has density of 1 g/cm^3 .

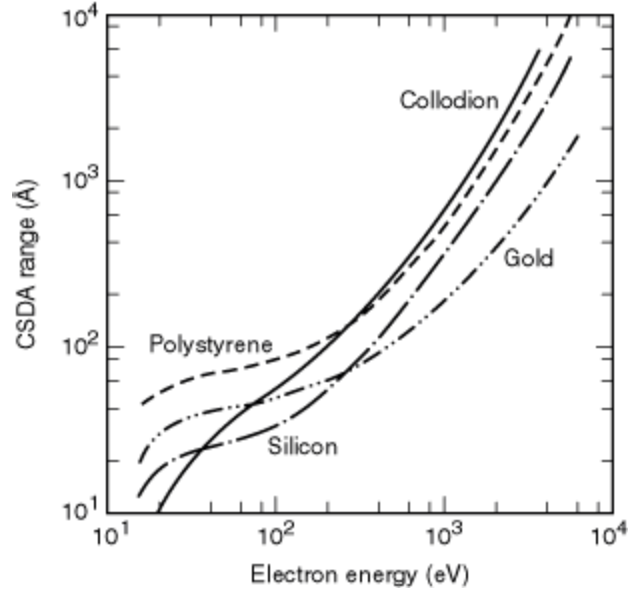


Figure 7 - Continuous Slowing Down Approximation Range for Gold, Silicon and Polystyrene [15]

Gamma rays and x-rays are photons (the electromagnetic radiation of high frequency). Photons interact with matter via the following processes: photoelectric effect; pair production; and Compton effect.

In the photoelectric effect, a photon is absorbed by an atom. One of the atomic electrons (a “photoelectron”) is released from the atom in this reaction. Free electrons cannot absorb photons and recoil. Therefore, the energy and momentum cannot both be conserved in such a process. Heavy atoms are needed to absorb the momentum at little cost in energy. The kinetic energy of the electron is defined by:

$$T_e = E_\gamma - B_e \quad (\text{Eq. 11})$$

Where B_e is the binding energy of electron and E_γ is the photon energy. The probability (cross-section) of photoelectric effect, σ_{pe} , is most significant for the low

energy photon (~ 100 keV). It shows discontinuous “jumps” at energies corresponding to the binding energies of electronic shells and it rapidly decreases with photon energies ($\sim E_\gamma^{-3}$) above the K-edge.

The pair production interaction method is the simultaneous creation of a subatomic particle and its antiparticle from another form of energy, especially the production of a positron and an electron from a gamma ray photon in a strong electric field, such as that surrounding a nucleus. The process energy balance is:

$$E_\gamma = T_+ + mc^2 + T_- + mc^2 \quad (\text{Eq. 12})$$

This process requires the nearby presence of a massive atom for momentum conservation, but the recoil energy given to the atom is negligible. There is the obvious photon energy threshold:

$$2m_e c^2 = 1.022 \text{ MeV} \quad (\text{Eq. 13})$$

Where the probability of σ_{pp} increases steadily with increases in energy, following:

$$\sigma_{pp} \approx Z^2 \quad (\text{Eq. 14})$$

The Compton or incoherent scattering is the elastic scattering of photons from free electrons. In matter, the electrons are bound. However, if the photon energy is much higher than the binding energy of the atomic electron, this binding energy may be ignored and the electrons can be considered essentially free. In the scheme shown in Figure 8, a gamma ray of energy $h\nu$ scatters from an electron with energy $h\nu'$ (all energies are expressed in MeV). The energy that the electron gains in this collision is T_e . Since the

total energy is conserved during the interaction, $h\nu = h\nu' + T_e$. The momentum is also conserved in the collision, and produces the following two expressions:

$$\frac{h\nu}{c} = \frac{h\nu'}{c} \cos \theta + P \cos \phi \quad (\text{X-component of momentum}) \quad (\text{Eq. 15})$$

$$0 = \frac{h\nu'}{c} \sin \theta - P \sin \phi \quad (\text{Y-component of momentum}) \quad (\text{Eq. 16})$$

Where P represents the momentum of the electron.

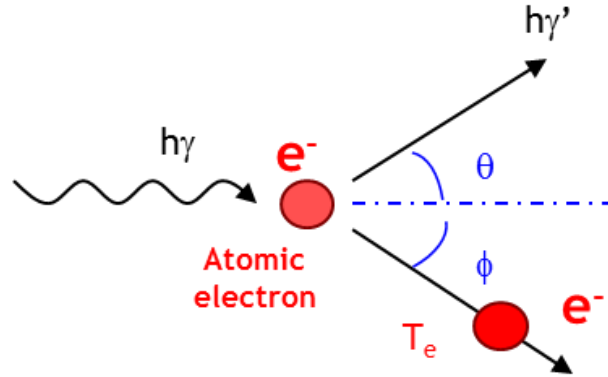


Figure 8 - Compton Scattering: θ and ϕ are the Scattering Angles for $h\nu'$ and Electron, Respectively [16]

Solving these equations:

$$h\nu' = \frac{h\nu}{1 + \frac{h\nu}{m_0 c^2} (1 - \cos \theta)} \quad (\text{Eq. 17})$$

and therefore

$$\lambda' - \lambda = \lambda_c (1 - \cos \theta) \quad (\text{Eq. 18})$$

Where λ_c is known as the Compton Wavelength:

$$\lambda_c = \frac{h}{m_e c} = 2.426 * 10^{-10} \text{ cm} \quad (\text{Eq. 19})$$

In Compton scattering, the photon interacts with individual electrons, so it is possible to define a Compton cross-section per one electron, σ_C . The σ_C decreases monotonically from the Thompson cross-section (σ_T) value at $E=0$ (0.665 barns, the maximum value) with increasing energy E . For energies significantly larger than the energy of the electron (E_e), σ_C behaves approximately as E^{-1} . The Compton cross-section per atom " σ_C " is $Z \times \sigma_C$. The shielding of Compton scattered gamma rays is a problem.

The relative importance of these three major processes in gamma ray interactions is shown in Figure 9.

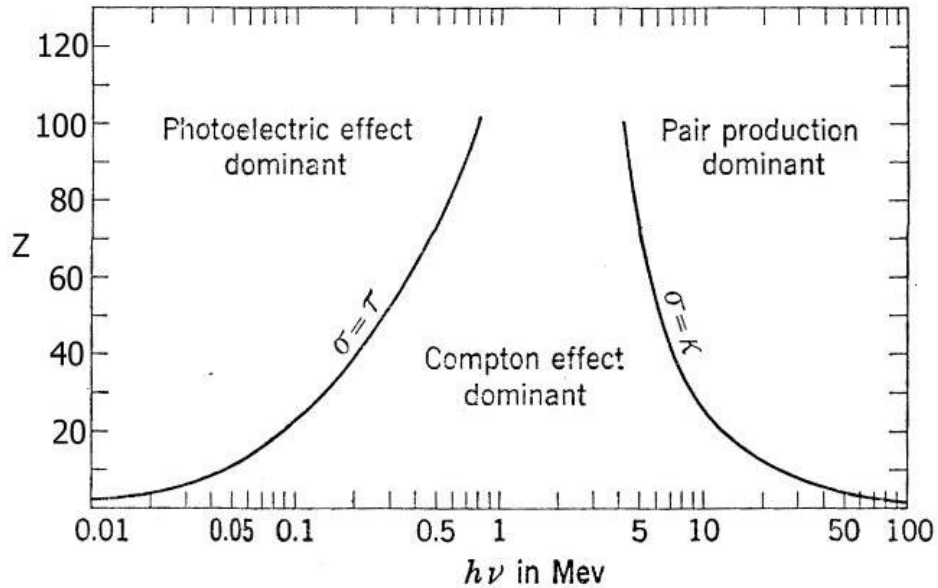


Figure 9 - Relative Importance of Three Major Processes [17]

Neutrons are not charged and interact with material by means of: 1) elastic and inelastic scattering; 2) radiative-capture; 3) charged particle reactions; 4) neutron producing reactions; 5) and fission. In the elastic scattering (n,n) interaction, a neutron hits the nucleus in its ground state (usually), then the neutron flies away. The nucleus is left in its ground state. Conversely, in an inelastic scattering (n,n') interaction, the neutron hits the nucleus in its ground state, then flies away, and the nucleus is left in an *excited* state. The nucleus receives energy from the neutron creating an endothermic process. The excited nucleus decays with the emission of “inelastic” gamma-rays. Figure 10 shows the scheme of an inelastic collision. The neutron in the scheme is represented by m_1 while the nucleus is represented by m_2 . The neutron approaches the nucleus with a velocity, v_1 , which is visualized in step (a). In step (b) the collision between the neutron and the nucleus has taken place, and the two travel at a new velocity (v_2) as a single mass element. During this process, the energy is transferred from the neutron to the nucleus, causing the nucleus to become excited. In step (c), the collision has completed and now the neutron separates from the nucleus and travels at a new velocity (v_3). The nucleus continues travelling at v_2 , but has now ejected some of the energy that caused it to be excited during the collision. This emitted energy is what causes the kinetic energy of the collision to not be conserved.

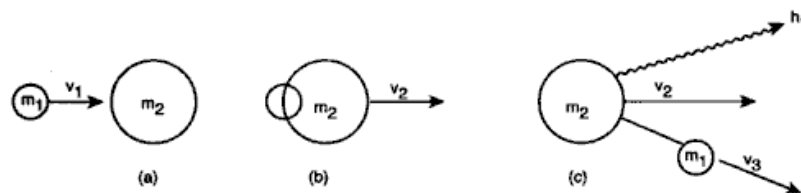


Figure 10 - Inelastic Collision Between a Neutron and a Nucleus [18]

In the elastic collision, the two particles (the neutron and the nucleus) collide and the kinetic energy is conserved. This means that as the neutron approaches the nucleus and, sequentially, collides with the nucleus, the neutron and the nucleus will travel at velocities that are equivalent to the ratio of their masses, following the momentum conservation. This process is visualized in Figure 11, which shows an elastic collision between a neutron (m) and the nucleus of an atom (m_2).

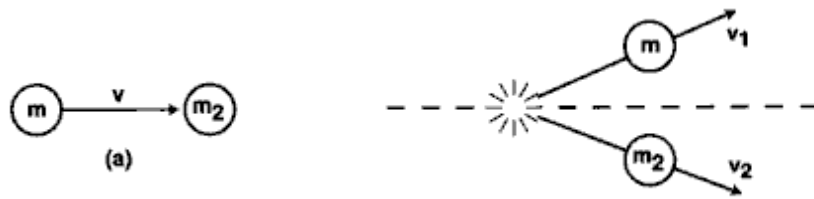


Figure 11 - Elastic Collision Between a Neutron and a Nucleus [18]

In the scheme, the neutron approaches the nucleus of the atom with a velocity, v . This is shown in step (a). After the collision, the two masses scatter in equal vectors from each other, with velocities that are equivalent to the ratio of their masses, following the conservation of momentum:

$$m * v = m * v_1 + m_2 * v_2 \quad (\text{Eq. 20})$$

In the case of the elastic scattering, due to the ratio of the masses, the neutron is likely retaining a majority of the energy that it initially had before the collision with the nucleus. For example, if m_2 is the atomic mass of ^{235}U , which is approximately

$235.04 \frac{\text{grams}}{\text{mole}}$ [11] and m is the atomic mass of the neutron, approximately $1.008664 \frac{\text{grams}}{\text{mole}}$ [11] then the resulting ratio would show that the ^{235}U atom is accounting for approximately 99.57% of the cumulative atomic mass in the collision. As such, to satisfy the law of the conservation of momentum, the velocity of the neutron, after the collision, must carry 99.57% of the cumulative velocity. Because of this, the neutron retains 99.57% of the kinetic energy it had before the collision took place, allowing for the neutron to still travel through the matter at high energies. This shows it could take several elastic scattering collisions to occur in order for the neutron to lose enough of its energy to be at a level where it can be absorbed into the nucleus it collides with.

In the radiative capture (n, γ) or neutron “absorption” process, the neutron is captured by the nucleus, and one or more “capture” gamma-rays are emitted. In charge particle reactions such as (n, α) and (n,p) reactions, the neutron is absorbed and then charged particles are emitted. These processes may be endothermic or exothermic. Contrarily, the neutron producing reactions (n,xn) are happening under the action of energetic neutrons and they are purely endothermic.

The fission reaction splits a nucleus into two parts with the particle and photon emission. Fission is, by definition, the act of cleaving or splitting into parts [19]. This reaction is accompanied with a large energy release, which is harnessed in nuclear power plants. Fission is usually induced by the collision of a neutron with that of a heavy atom’s nucleus, such as the fissionable fuel of choice – ^{235}U . Figure 12 shows a typical fission event involving ^{235}U . In Figure 12, the neutron is absorbed by the ^{235}U nucleus in Step A. The absorption of the neutron causes the ^{235}U nucleus to convert to Uranium-236 (“ ^{236}U ”)

following the equation displayed in Equation 21. The result is then a ^{236}U nucleus that is unstable and fissions to two lighter nuclei.

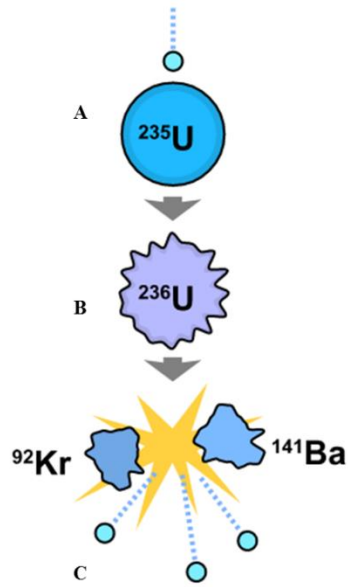
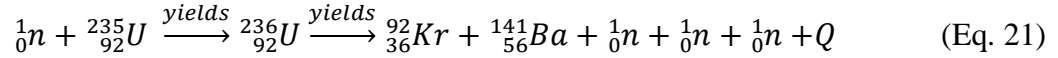


Figure 12 - Fission of ^{235}U Nucleus [20]

In Step C, the ^{236}U nucleus splits into Krypton-92 (^{92}Kr) and Barium-141 (^{141}Ba) along with three neutrons that can continue this event in other ^{235}U material. The resulting energy release, Q , is the energy that it took to hold the ^{236}U nucleus together, and as a result of the fission, the energy is released into the surroundings, typically as heat.

Not all fission events of ^{235}U result in the production of ^{92}Kr and ^{141}Ba as the by-products. Figure 13 shows the relationship of the probability of each of the possible fission products in relation to the molecular weight of the fission products. The X-Axis

shows the molecular weight while the Y-Axis shows the probability of the fission event resulting at that molecular weight.

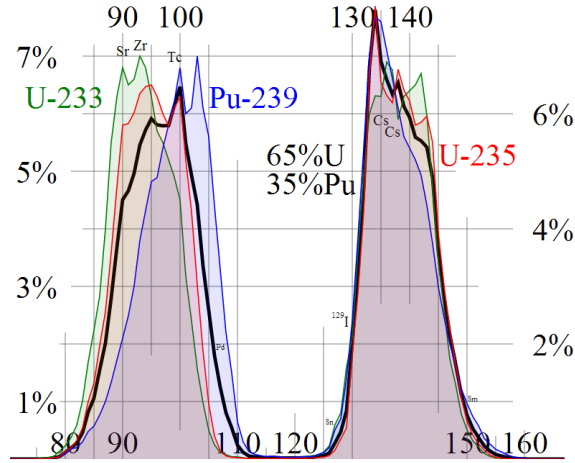


Figure 13 - Products of Thermal Neutron Fission of ^{233}U , ^{235}U , and ^{239}Pu [21]

Each of these interactions, scattering and absorption, are all characterized by their cross-sections. In Figure 15, the absorption cross-section is plotted with the elastic scattering cross-section and the total cross-section of ^{235}U . In the figure, it is clear that as the energy increases, the cross-section for absorption decreases. Conversely, the elastic scattering cross-section stays relatively constant throughout the energy spectrum. But as the energy of the neutron increases, the chances that the neutron will elastically scatter are higher than the chances that it will absorb into the nucleus.

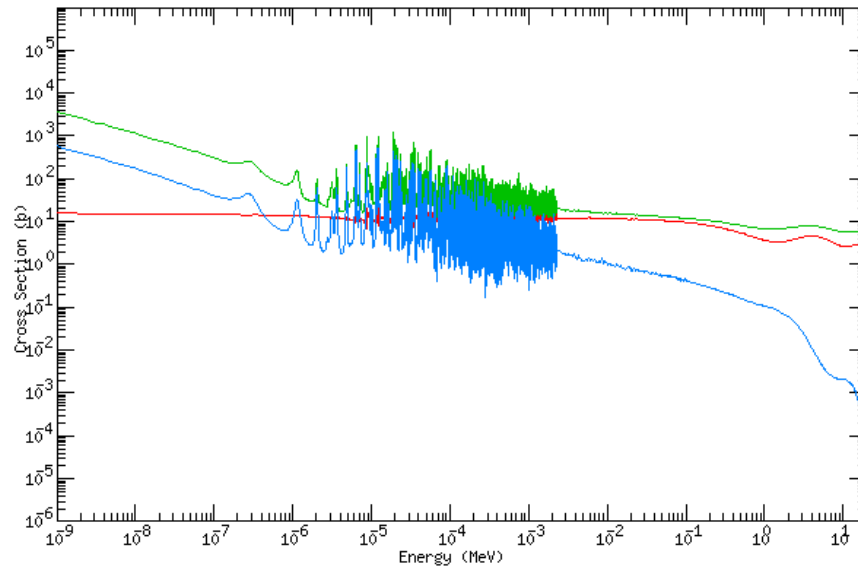


Figure 14 - ^{235}U Cross-Section Data; Total Cross-Section (Green), Total Absorption Cross-Section (Blue), Elastic Cross-Section (Blue) [11]

Because the probability of neutron absorption is higher at lower energies, most neutron-capture-based detector systems require a step that will cause the energetic neutron to lose enough of its energy to adequately interact with the detector material. This step is known as moderation, and is employed in many detector systems in the use today, specifically with the Helium-3 detectors.

The reason Helium-3 is the choice material for neutron-capture based reactions is that it has a very high absorption cross section at thermal energies, shown in Figure 15. This high cross section makes the Helium-3 detector system very reliable in measuring neutrons in environments where the neutrons have been adequately moderated.

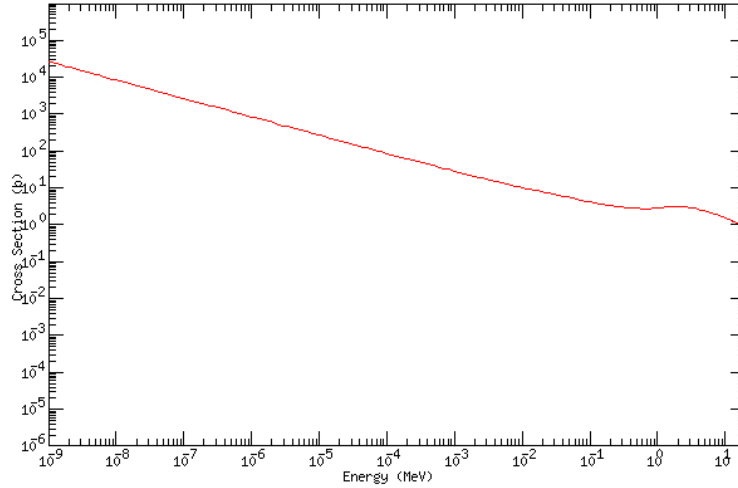


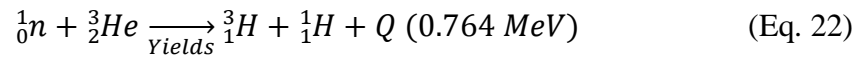
Figure 15 - ^3He Total Absorption Cross-Section Data [22]

1.4.3 Neutron Detection Technique

Neutron detection is based on the interaction processes between the neutrons and the detector material. As an example, consider a typical ^3He gaseous detector. In the detector, the ^3He gas is used as the detector material. The moderator material is typically surrounding the counter. The neutron energy loss is also happening within the gas volume. As the low energy neutron enters the ^3He gas, it collides with the molecules of the gas mixture. As with the example of elastic scattering with ^{235}U , the neutron will scatter inside the ^3He gas until enough of its energy has been lost, such that the neutron is in the thermal equilibrium with the environment. As previously discussed, the atomic mass ratio between a neutron and an atom of ^{235}U is 99.57% in favor of the ^{235}U atom. With the ^3He atom, the ratio is much smaller. An atom of ^3He has a density of approximately $3.016 \frac{\text{grams}}{\text{mole}}$ [22]. When comparing this atomic mass to that of the neutron ($1.008664 \frac{\text{grams}}{\text{mole}}$), the ratio amounts to be 66.55% in favor of the ^3He atom. This means

that for the scattering collision the neutron has inside the ^3He gas, it will lose approximately one-third of its energy, which in turn translates to less collisions are required for the neutron to reach the thermal energy spectrum, where it can now be captured by the ^3He nucleus.

With its energy lost through scattering collisions with ^3He nuclei, the neutron is more likely to be captured by a ^3He nucleus. As a result, the following reaction takes place:



In this reaction, the absorption of the neutron by the ^3He causes the production of triton and proton. These moving ions are detected through an electrical charge produced by them within the gas volume. The trail of electron-ion pairs created by moving proton and triton is then accelerated by the electric field of a proportional counter. Because the electrons are lighter than positive ions, they may be accelerated up to energies enough to start the avalanche multiplication of additional electrons. This process assists in amplification of the initial ionization charge. The scheme of avalanche development around a thin wire of the counter is shown in Figure 16

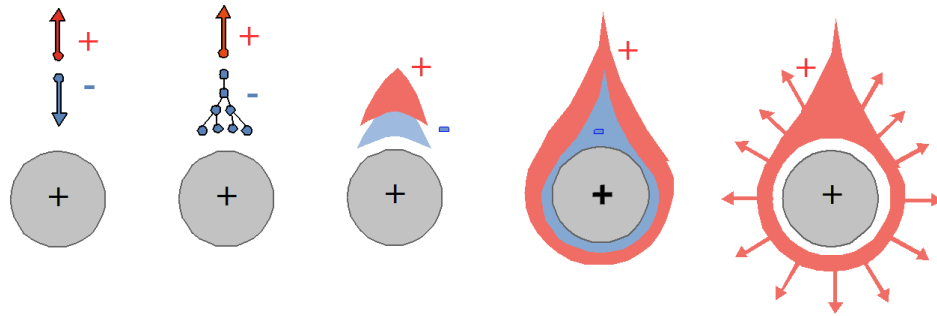


Figure 16 - Avalanche Development Around a Thin Wire of Gaseous Counter [12]

The current signal generated by the motion of electrons and ions in the anode wire is converted into an analog voltage waveform that is processed by the analog or digital signal conditioning electronics.

1.5 Scintillator Detectors

The technology studied in this work, is slightly different. With scintillators, either organic or inorganic, the method of detections is based on the process of luminescence, whereby light of a characteristic spectrum is emitted following the absorption of radiation. In this process, the emitted luminescence is usually less energetic than that of the absorbed radiation and thus requires a process of photon amplification through the means of optical readout devices such as photomultiplier tubes.

In the scintillation process, a particle of radiation excites the atom and a photon released from the de-excitation of the atomic electron can be observed. However, it takes significantly more energy to produce a scintillation photon than what is required to produce one electron-ion pair, typically 1 photon per 100 eV of dE/dx . In addition, scintillation materials re-absorb their own scintillation light. To correct for this, manufacturers often add doping atoms to “solve” this problem.

Scintillators are classified as either organic or inorganic. For organic scintillators, the organic molecules are typically of low density materials ($\rho \approx 1.3$ g/cc) such as Naphthalene or anthracene. In organic scintillators, the excitation radiation causes the non-radiating de-excitation to the first excited state which causes a scintillating transition to one of the many vibrational sub-states of the ground state. Direct transition to the ground

state is forbidden. Molecules cannot re-absorb the scintillation photon unless it was already in this particular vibrational sub-state. This causes the emission of a fast scintillation of light, with a de-excitation time of approximately 10^{-8} seconds. Organic Scintillators are often used with wavelength shifters to avoid absorption in light guides.

Inorganic scintillators have a much higher density than that of organic scintillators (i.e. $\rho \approx 3.6$ g/cc for NaI based detectors) and as a result, carry a much higher stopping power. One such inorganic scintillator is a thallium-activated Sodium-Iodine (NaI) scintillator. In the inorganic scintillator, the excited electron in the conduction band can fall in a luminescence level, resulting in the emission of a non-radiative phonon. The de-excitation time of inorganic scintillators is much slower than that of organic scintillators, measuring approximately 10^{-6} seconds. Because of this lag, the organic scintillator was chosen as the detector medium of choice for this project.

1.6 Time Correlation Measurements

Time-coincidence measurements, is based on the idea that detections can be made on two or more detectors using the same time base from the same source of multiplicity. Figure 12 shows an example multiplicity measurement study. Notice in Figure 12, taken from [23], that four detectors are placed equally around the perimeter of a point source. This allows for radiation to be detected at multiple points from the source, which when taken together can determine many important facts about the radiation such as time of arrivals, energy, decay rate, etc.

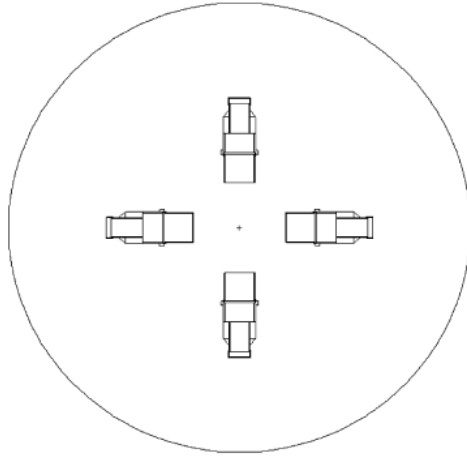


Figure 17 – Example of Neutron Multiplicity Measurement System [23]

CHAPTER 2

LITERATURE REVIEW

The economic shortfalls of the ^3He gaseous detectors, specifically the shortage of supply gas, are not a “new” threat to the neutron detection industry, as it has been the motivation for several advances in neutron detection technology. In [3] two scientists studied the shortage of Helium-3 supply, and how it affects the nuclear community. In their work, the authors wrote about the dwindling supply of Helium and the increase of demand due to the events of September 11th, 2001, which caused a rapid deployment of several detectors to secure the United States borders. This ultimately led to massive price hikes in Helium 3 based systems. The authors, Dana A. Shea and Daniel Morgan, go on to say that policymakers in the government, now face a number of difficult decisions, starting first with how to adequately allocate the dwindling supply of Helium-3. The authors state that “For example, some types of cryogenic research can only be accomplished with Helium-3, whereas in medical imaging and neutron detection, helium-3 has advantages but also alternatives.” In this statement, it is clear that even though Helium-3 has advantages in the neutron detection industry, it will be rather low on the list in consideration for receiving Helium-3 supply from the government.

The shortage of Helium-3 supply is not just a national issue, but is also international as several countries have detectors systems and research projects based on the use of Helium-3. Consider the case with the Japan Accelerator Research Complex (J-PARC), based in Tokai, Japan, which was supposed to be one of the leading facilities of its kind, allowing an unprecedented view of microstructures in life and physical sciences. However when the \$1.5 billion facility opened in 2009, it was missing something

important: Helium-3. In [24], Cartwright explains that the J-PARC facility requires 100,000 liters of Helium-3 to operate, and in 2012 the facility had only acquired 85,000 liters. As a result, the facility was left nonoperational.

This shortage of Helium-3 supply has spurred on a race in recent years for scientists and engineers to develop new and accurate means of neutron detection, without requiring the use of Helium-3. Countless numbers of scientific reports, journals, and techniques have been developed. In the following sections, some of these methods are discussed along with other works that dealt with the scintillation-based technologies.

2.1 Helium-3 Alternatives

Multiplicity counters are just one example of a neutron detector that is affected by the shortage of Helium-3 gas and is discussed by Lintereur et al in [25]. In his research, Lintereur et al. discusses two options of replacement technology for the Helium-3 gas technology. The alternatives that are suggested are Lithium-6 (^6Li) and Boron-10 (^{10}B). This is accomplished through three forms of detector systems: 1) using ^6Li in the form of Lithium-Fluoride (^6LiF) material; 2) using ^{10}B in the form of Boron-Trifluoride ($^{10}\text{BF}_3$) gas; or 3) using ^{10}B in a solid-powered form, lining proportional counters. The theories put forth by Lintereur et al. are also substantiated by several other reports and journals.

One such example of support for [25] is found in [26] a report submitted to the United States Government Accountability Office, in September of 2011, written by Timothy M. Persons and Gene Aloise. In [26], the scientists point out the shortage of Helium-3 available to the scientific community, and also suggest that ^{10}B and ^6Li based

technologies offer reliable alternatives to Helium-3, confirming the research shown in [25].

Where the two papers differ however is in the application. In [25], Lintereur simulated the three technologies and discovered that each one has their respective disadvantages. For example, in regards to the BF_3 gas counters, it was found that the detector systems would require one of three major changes to overcome efficiency losses. The first option would require that significantly more detector tubes containing BF_3 gas would be required. However in doing so, the system's footprint would have to increase and the neutron "die-away" times would increase as a result of larger distances to travel. Likewise, the second option (increasing the volume of each BF_3 tube) would result in the same outcome. The last option, for Lintereur, was to increase the pressure of each BF_3 tube. With increasing tube pressure, though, would require larger amounts of voltage to be supplied to the system and the voltage will ultimately limit the available pressure.

Conversely, in [26], Persons states that BF_3 showed remarkable efficiency in radiation portal monitors (RPMs). The problem with using this technology in this application is that BF_3 gas is a "mature technology for other detector applications." Persons goes on to say that BF_3 gas must be integrated into mature prototypes of radiation portal monitors, although this work has not been done yet.

[25] and [26] both continue to discuss the remaining two alternative technologies, and again point out the disadvantages to using these technologies in their particular applications. [25] concludes that the highest performing alternative is that of LiF/ZnS sheets as the alternative mode for neutron detection.

Several articles, reports, journals and papers come out in support of the ideas presented by [25] and [26]. However, what many of them leave out is the fact that these technologies maintain many of the properties similar to that of the Helium-3 detector systems. For example, in [27] Michael Erickson of Los Alamos National Labs wrote, “Unlike Boron Trifluoride (BF_3), a hazardous gas that has been suggested as a Helium-3 replacement, Boron-10 (Boron-10 lined Proportional tubes) are non-toxic and pose no environmental danger.” Erickson rallies to argue that Boron-10 technologies are intelligent because they provide excellent gamma/ neutron discrimination and there is a vast supply of Boron-10 in stockpile. Erickson’s statements are confirmed by A.P. Simpson et al. with the Institute of Nuclear Materials Management (INMM) in [28].

What is important to take away from [25], [26], [27], and [28] is that each of the references refer to alternatives that rely on moderation techniques before the detection of neutrons can take place, one of the major disadvantages of the Helium-3 detector systems in comparison to plastic scintillators. With that step included in the system, the detector system must have the space necessary to accommodate enough of the moderating material to adequately moderate the neutron without actually interfering with the actual detection mechanism. This leads scientists in the direction of using relatively advanced, alternative technologies that offer improved count rate statistics in faster intervals, such as scintillators.

2.2 Review of Neutron Detection with Scintillators

In [29], author Sy Stange makes a very compelling point when it comes to neutron detection with Liquid Scintillators. Stange et al. states that Helium-3 detectors are used in the non-destructive assay of special nuclear material because of their

sensitivity to thermalized neutrons, however, fission neutrons must be moderated before the detection can occur. In addition to this, the authors point out the serious disadvantage of the high count rate limitations imposed by the Helium-3 detectors, stating that the typical coincidence gate lengths are on the order of tens of microseconds. Conversely, liquid scintillators would detect fast neutrons making it possible for the coincidence gate lengths significantly smaller, on the order of nanoseconds. Because of the shorter gate lengths, Stange et al. state that accidental coincidences between detections are less common, and lead to the ability of being able to detect neutrons with a greater accuracy and in less time. In [29], the researchers use GEANT Monte Carlo Simulation to determine the results of a liquid scintillator multiplicity counter, and then experimentally perform the measurements to establish a benchmark for the technology.

One of the most widely used liquid scintillator materials is the BC501A neutron detector, as discussed by N. Patronis et al in [30]. In [30], the authors summarize the BC501A organic liquid scintillator, stating that it is commonly used for neutron monitoring, time-of-flight measurements, and neutron spectroscopy measurements. The task of [30] was to model the BC501A neutron detector in GEANT and use Monte Carlo to predict the efficiency of the BC501A detector at various neutron energies.

A critical point for this research comes from the “on-line” analysis of the detected signals. This analysis is done by analyzing the pulse shape differences between neutrons and gamma-rays, and is specifically discussed by Shiping Li et al. in [31]. In [31], Li states that pulse shape discrimination is necessary to adequately separate gamma-rays and background radiation (such as alpha particles and cosmic neutrons) from neutrons in a fission environment. However, Li et al. states that the common analysis models are not

adequate for the Neutron Flux Monitor environment, and analysis must be done on the amplitude of the scintillation in addition to the rise time of the signal. In addition to this, they point out that analog pulse shape discrimination techniques are limited by low maximum count rates, and the changes made in the technical field have allowed for the development of n/γ discrimination algorithms suitable for FPGA embedding, which allows for the real-time analysis of the detected digital signals. What makes the FPGA so useful in this particular application is that it allows one to select only pulses larger than the threshold and truncate them, retaining the significant parts of each pulse, which is discussed in [32].

In addition to the development of state-of-the-art field-programmable-gate-arrays, today's high performance circuits for Analog-to-Digital Converters (ADC) have allowed for the FPGA's to be used to their full extent. These high speed ADCs enables a spectroscopy system to process high-count rate signals from multiple detectors. In [33], authors Pil Soo Lee, Chun Sik Lee, and Ju Hahn Lee, show a "proof-of-principle" model in which they developed a FPGA-based digital signal processing system for the task of measuring pulse heights and rise times "on-line". Lee et al. were able to perform measurements of the pulse heights and rise times of detected signals and process them by means of a digital filtering process and pulse-shape discrimination analysis. The authors were able to successfully show the process in an alpha-gamma measurement, which suggests the importance of adequate ADC conversion and FPGA programming, both of which are equally necessary in experiments conducted in this thesis. Many other important attributes of the FPGA systems are discussed in [34], [35], and [36].

In [37], the authors take measurements using a liquid scintillator material to the next level, by using EJ-301 and EJ-309 materials, the liquid versions of the plastic materials used in the experiments for this thesis. In [37], Stevanato et al. attempt to show the reliability of the EJ-309 liquid scintillator to that of the EJ-301 liquid scintillator. Furthermore, they show that the two liquid scintillators have a remarkable ability to identify weak neutrons in a high gamma-ray background environment. The authors discuss that liquid scintillators are often used for fast neutron detection because of their pulse shape discrimination abilities which is used to separate the neutron from the gamma-ray. Liquid scintillators have found a place in Homeland Security applications. For this reason, Stevanato et al. set out to test the materials by detecting a weak neutron in a high gamma-ray environment. They found however, that if the PSD Analysis is done in on-line mode only, that many “fake” neutrons will be seen by the analyzer. When the results are analyzed, off-line, Stevanato et al. found that many of the FPGA components could be rejected to clean up the detection, thereby witnessing the weak neutron measurement.

Recently, there has been a push into the field of using plastic (solid)-state scintillators in place of their liquid counterparts. This is because the solid scintillating material is far more stable than that of the liquid, and non-toxic. Ulisse Braver and company performed measurements using a position-sensitive plastic scintillator detector for the purpose of fast neutron imaging in [38]. The detector was developed as a compact, plastic scintillator detector for the purpose of being a detection component for the Fast Neutron Imaging Telescope (FNIT), meant to detect neutrons ranging from 2 MeV to 20 MeV. According to Braver et al. the FNIT is used to measure neutrons emitted from the

fusion events taking place in the sun. With the telescope, there was a need to detect fast neutrons since many of the lower energy neutrons do not arrive to earth in significant quantities. Braver et al. contest that the detector would have wide sweeping impacts on the spectroscopy of special nuclear material, due to the penetrating neutron emission of fissionable material.

2.3 Review of Neutron Multiplicity Measurements

Because the time correlation study of multiple detected gamma-rays is a major part of this thesis, it is important to review work done with Multiplicity Counters that are specifically designed with scintillator detectors. In [23], Andreas Enqvist et al. wrote on the characterization of mixed multiplicity counters using liquid scintillators. In their work, Enqvist et al. highlight the common theme with the decision to venture in the scintillation technologies as viable alternatives to Helium-3 multiplicity counters. They continue by describing the characteristics of a multiplicity counter of fission neutrons using liquid scintillators, continuing from previous cross-correlation measurements of a Californium-252 (^{252}Cf) which are summarized in [39] and [40]. Enqvist et al. found that the measurement system was very accurate in discriminating neutron pulse from gamma-ray pulses, which allowed the system to gather measurement data for several reactions in a relatively short amount of time.

In [41], the authors documented the work done on a collaborative project between Idaho National Laboratory and the University of Michigan. In the project, D.L. Chichester et al. states that the purpose of the project was to “examine design parameters related to the use of fast-neutron multiplicity counting for assaying plutonium for materials protection, accounting, and control purposes.” They propose that the fast

neutron multiplicity counter using the EJ-309 liquid scintillator material has three potential benefits: the ability to significantly reduce assay measurements times, significantly improve assay precision, and lastly moderately improve both measurement precision and durations over current technologies.

These sources however mean nothing without understanding the analysis methodology of multiplicity measurements, which are documented in [42] and [43]. In [42], the author documents a technique that can be used to compute the statistics of the neutron counting distribution, while in [43], the author documents a fully digital list-mode data acquisition which allows scientist to digitally record the detection time of each neutron.

Mattingly, discusses previous models that have been used, going from point models, in [44] – [50], then moving to discuss the use of Monte Carlo Models, which allows for Mattingly to simulate the average neutron population (which is what point models simulated) and the fluctuations in the population that result from multiplicity emissions of neutrons during fission, seen in [51] – [53]. Mattingly continues by documenting many of the transport equations for neutron multiplicity.

Likewise, Ridnik et al. documents how list mode data acquisition can be used for multiplicity counting, looking specifically in determining fissile mass based on multiplicity measurements. In order to accurately estimate fissile mass, spontaneous fissions sources must be separated from additional neutron sources which are done by solving a set of three equations for three unknowns [54]. Using this information, and

analyzing the list mode data, offline, allows for Ridnik et al. to calculate the dead time corrections for measured multiplicity moments.

CHAPTER 3

EXPERIMENTAL STUDY

3.1 Component Descriptions and Specifications

3.1.1 Scintillating Materials

First and foremost is the most crucial part of the detector: the plastic scintillating material. The material of choice was chosen to be the EJ-299-33 and EJ-299-33A plastic scintillating materials manufactured by Eljen Technologies. This particular scintillating material was selected because it was and still is a “revolutionary plastic scintillator (that) possesses pulse shape discrimination properties enabling the separation of gamma and fast neutron signals on the basis of their timing characteristics using conventional PSD electronics systems [55].” The scintillator is still in the development phase, as Eljen Technologies is optimizing the composition of the material and the manufacturing process, which led to the manufacturing of the 33A material. Table 3 shows the physical and scintillation constants for the EJ-299-33 material. It is important to note the light output and the scintillation efficiency of the scintillating material, as these two quantities show the light output of the scintillating material as it compares to anthracene (in %) and the efficiency of each scintillation in regards to the number of photons detected per 1 mega-electron-volts (MeV) of electron excitation.

Table 3 - EJ-299-33 Scintillator Parameters [55]

Physical & Scintillation Constant	Value
Light Output (% Anthracene)	56
Scintillation Efficiency (photons/ 1MeV e^-)	8600
Wavelength of Maximum Emission (nm)	420
Hydrogen Atomic Density (H atoms/ cm^3)	$5.13 * 10^{22}$
Carbon Atomic Density (C atoms/ cm^3)	$4.86 * 10^{22}$
Electron Atomic Density (Electrons/ cm^3)	$3.55 * 10^{23}$
Density (grams/ cm^3)	1.08

Most of the experiments in this thesis were done using the EJ-299-33A scintillating material which, as the name suggests, is a revised iteration of the original EJ-299-33 material. The two materials are physically the same, where the 33A material has almost the same properties as the 33 materials. The difference comes in the further optimization of the manufacturing process by Eljen Technologies. With the revised material, the manufacturing process was improved and optimized the physical appearance of the material. The two materials, the EJ-299-33 and the EJ-299-33A, are shown in Figures 18 and 19. A side-by-side comparison is also included in Figure 20, to demonstrate the difference between the two materials. Because the properties of the material remained the same through both iterations, the results varied minimally between tests conducted on both materials, which led to the use of the 33A material in many of the experiments.



Figure 18 - EJ-299-33 Plastic Scintillating Material



Figure 19 - EJ-299-33A Plastic Scintillating Material

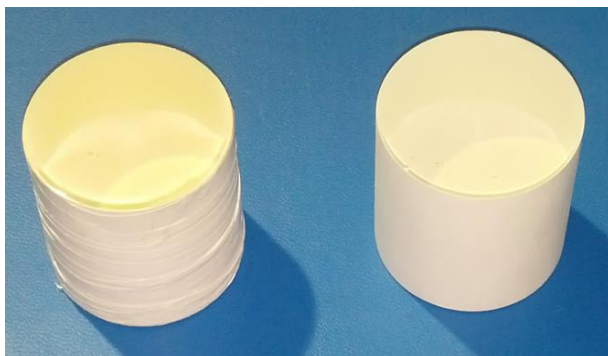


Figure 20 – EJ-299-33 (Left) and EJ-299-33A (Right) Comparison

The EJ-299 materials shown in Figures 13 and 14 are both 2-inches (in) in diameter, and stand at a height of 2 in.

3.1.2 Photomultiplier Tube

In order to detect and quantify the light scintillations emitted by the scintillating materials, a photomultiplier tube (PMT) is coupled to the surface of the plastic EJ-299 scintillating materials. For this task, the PMT was selected to be the stage model B51B03W manufactured by ADIT. This particular model is a 2-in, 10-stage high gain photomultiplier tube, specifically design for scintillation counting. What makes this model very unique is that it best used in environments where high count rates are necessary. Because the scintillating materials made by Eljen Technologies are all fast neutron and gamma-ray detectors, their time between each triggered event (detection of a particle) is much shorter than the gaseous-counters. Therefore, they require a PMT that will allow for this advantage to be used, and the ADIT PMT allows for this application while retaining high count rate efficiency. Figure 21 shows the design schematic of the ADIT B51B03W PMT. Because the scintillating material's diameter is 2-in, the PMT perfectly aligns with the scintillating face of the EJ-299 materials, which allows for the establishment of a "light-tight" environment between the interfaces of the two components.

Figure 21 shows two build options for the ADIT B51B03W PMT. One option comes with the pinouts as regular wires while the other comes with the pinout base. With the pinout base, the pinouts wires are pre-soldered to their appropriate connections,

allowing for the easy communication between the PMT and the data acquisition board (DAQ). In addition, the pre-soldered version of the PMT offers the insurance of being professionally constructed, which decreases the probability of having communication issues between the DAQ and the PMT.

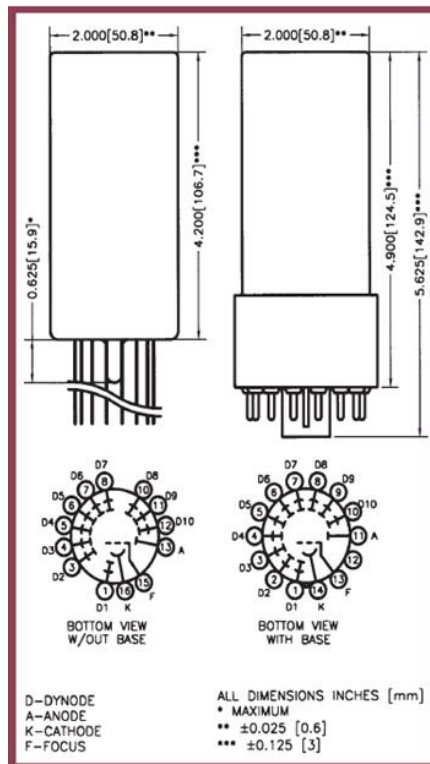


Figure 21 - Design Schematic of the ADIT B51B03W PMT [56]

It was mentioned that the B51B03W PMT has a remarkable sensitivity to detections made in high count rate environments. In addition to this, the ADIT PMT has a remarkably high sensitivity to neutrons at the value of the wavelength output from the plastic scintillator. In Table 3, it was shown that the wavelength of the light scintillation is approximately 420 nanometers (nm). According to the ADIT statistical information, the B51B03W PMT has a remarkable efficiency and sensitivity to detections at about 380

to 400 nm. This information is shown in the graph in Figure 22. This graph shows the absolute sensitivity of the B51B03W PMT along with the Quantum Efficiency of the PMT at various wavelengths. The mark (green) in Figure 22 shows the wavelength value of the EJ-299 scintillation materials.

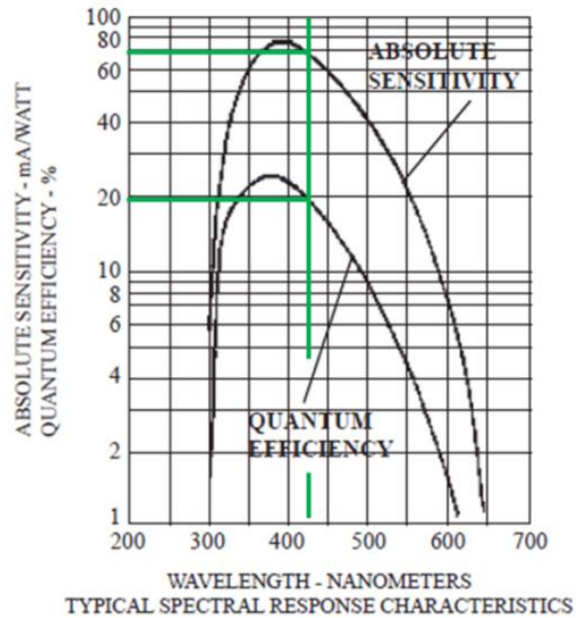


Figure 22 - Absolute Sensitivity & Quantum Efficiency of B51B03W PMT [56]

From the information shown in Figure 22, it is clear to see that the ADIT B51B03W PMT retains high efficiency and sensitivity at the output wavelength of the EJ-299 scintillating materials, making them an ideal choice to use in conjunction in the overall assembly of the scintillator detector. Figure 23 shows the actual PMT product from ADIT which was used in each of the scintillators constructed.



Figure 23 - B51B03W PMT by ADIT

3.1.3 Data Acquisition

In order to control the detector applications and read control outputs, a digital data acquisition device must be used. The eMorpho Data Acquisition Unit (DAQ) shown in Figure 24 accomplishes this task.



Figure 24 - eMorpho Data Acquisition Device from BPI [57]

The eMorpho system is powered solely through the USB 2.0 interface with the computer system, which allows for the convenient connection with the scintillator detectors. However, what makes this product so ideal for this particular application is that it requires no preamplification of the data signal, meaning it can be directly connected to the PMT anode. The eMorpho system requires a current supply of just 265 miliamperes (mA) with a supply voltage between 3.3 volts (V) and 5.5 V [57]. This data acquisition system allows for the use of high voltage, amplifying the supply voltage to upwards of 1,100 V to supply power and amplify the signal detected from the PMT, all of which is accomplished by the USB interface with the computer. The final benefit of this device is that the eMorpho system has the ability to perform Pulse-Shape Discrimination analysis on the detected signals to allow for pile-up rejection and for particle identification based on the timing properties of the detected signal.

The device converts the current signal output from the anode of the B51B03W PMT to a voltage signal with a programmable gain, while also preserving the pulse shape of the anode output. The converted analog voltage signal is then processed by a 12-bit, 100 mega-hertz (MHz) waveform-digitizing Analog-to-Digital Converter (ADC). The result is a digital image of the pulse waveform. This waveform is then sent to the XC3S200 Programmable Logic Gate Array (FPGA), which executes the digital signal processing in real-time, and viewed through the connected computer. The data is then stored in an embedded signal processor that carries a 128 kilobyte (kB) non-volatile memory and hosts a modular firmware and software design, allowing for easy access to the list mode data through the interface with the computer. The multichannel analyzer has 4,096

channels for the spectral analysis of the detected signals, meaning that it can perform the detection in high count rate environments.

What makes this system truly convenient for use with this application is the fact that all of the analyses can be done online or “on-the-fly”. This means that as the system is performing the detection tasks, the user can perform analysis on the detected signals especially the pulse-shape discrimination analysis of the signals and the time-coincidence of detected particles.

In addition to the eMorpho data acquisition device, BPI also carries the 4-channel version of eMorpho, commonly known as qMorpho. qMorpho is essentially four eMorpho devices lined up in parallel allowing for the accurate measurement of multiplicity detection. The product is shown in Figure 25.



Figure 25 - 4-Channel DAQ: qMorpho

With the qMorpho system all controls and readouts with the device are done through the standard USB 2.0 communication interface. However, power for the qMorpho comes from an additional power supply. The qMorpho system then lowers the supply voltage to the nominal 3.3 to 5.5 V that the system requires [59]. As with eMorpho, qMorpho allows for the application of high-voltage amplification to each of the four channels on the qMorpho through the USB interface with the computer, separately from one another.

Both of these products were used in conjunction with the detectors that were constructed. The eMorpho was used to show the PSD application of the EJ-299 scintillating materials, while the qMorpho was used to support the multiplicity study of the detector arrays.

3.1.4 Graphical User Interface (GUI)

In order to display all of the digital aspects of the detector system, a simple graphical user interface (GUI) was implemented. The Morpho products discussed in the previous section all use the a pre-built GUI that is based on the IGOR PRO programming interface that is made by WaveMetrics Inc. [58]. The IGOR PRO environment is an open-source environment that allows for easy programming and analysis of scientific and engineering measuring devices.

What makes this environment so ideal for the data analysis portion of the experiments is that the open-source format of the environment allows for the user to alter programs easily, to allow for the access of point specific data that is stored in the measurement hardware. By accessing the list mode data of the hardware, IGOR PRO can

then analyze the information into many different types of graphics that can be used to accurately display the information. Furthermore, because of the open-source format of the GUI, IGOR PRO can access almost all types of data formats, making it quite convenient in accessing data of multiple types and formats.

As mentioned, BPI wrote the command program for the eMorpho and qMorpho systems in the IGOR PRO GUI environment. Through the GUI, the user can establish communication and control with the data acquisition system, view the detected particles, and perform “on-the-fly” digital analysis of the stored waveforms from the FPGA. What’s more is that because of the open-source format of IGOR PRO, the can be altered and reprogrammed to perform various user-defined tasks that were not previously defined, without the risk of affecting the overall programming code for the communication and control with the Morpho products.

3.2 Detector Assembly

Because the PMT is sensitive to emissions of light, in order to ensure that the PMT only sees the scintillation, the detector must be assembled in such a way that encases the PMT and scintillator in a “light-tight” environment. The first step taken to ensure that this condition was met was to surround the cylindrical wall of the PMT with a layer of black electrical tape, while leaving the circular face of the PMT uncovered. This ensures that any light emissions seen by the PMT will be originating from its circular face. With the circular face of the PMT interfaced with the scintillator material, it is reasonable to assume all light emissions seen by the PMT will have originated within the scintillating material.

To further ensure the creation of a “light-tight” environment, the PMT and the scintillator were encased in two aluminum enclosures, one that was designed to enclose the PMT and the other designed to enclose the scintillator. This provides the detector with two distinct advantages, A) creation of a “light-tight” environment within the enclosure, and B) a means of permanently maintaining a constant connection between the scintillator and the PMT without causing damage to the components.

With regards to the PMT enclosure, the piece of aluminum is open on both ends, allowing for the scintillator to be connected to the face of the PMT, through the combining of their enclosures, and for the PMT to be connected to the eMorpho, through the pinouts on the base of the PMT. The base of the PMT was also coated with a layer of black electrical tape, such that the tape held the PMT in a locked position with reference to the enclosure. Also, this sealed the PMT within the enclosure, making the environment a closed system thus blocking out light interference.

In regards to the enclosure of the scintillating material, the part was designed such that there would only be one opening, allowing for the interface connection between the PMT and the scintillating material. The other end was kept as solid aluminum. This face of aluminum was designed to have a thickness of 0.25 millimeters (mm), or approximately 0.01 inches, which would not interfere in the detection of neutrons or photons. A picture of the detector assembly is shown with the eMorpho in Figure 26.

At the point of interface for the PMT and the scintillator material, a small amount of clear Saint-Gobain electrical gel was applied. The Saint-Gobain acts as an impact protection layer between the two major components of the detector. This gel allows for

the two faces to be connected without causing damage to the components. In addition, the gel is clear and causes little to no interference between two components, allowing for accurate detection. Lastly, within each enclosure, the PMT and the scintillator are surrounded by a thin rubber O-ring, which is used to ensure the two faces do not change position in reference to each other, within the enclosure.

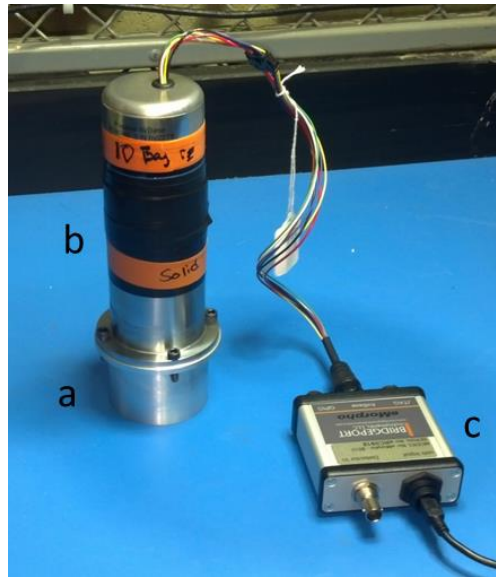


Figure 26 - Plastic Scintillator Detector: (a) the Scintillator Enclosure, (b) the PMT Enclosure, and the (c) eMorpho Hardware

3.3 Laboratory Environment

The neutron detector assembly equipped with the digital PSD system (eMorpho) was utilized to carry out radiation measurements using sealed photon and neutron sources. First, a source of Cobalt-60 (^{60}Co) measuring 0.1-micro Curies (μCi) and a source of Cesium-137 (^{137}Cs) measuring 0.1- μCi were each used as a means to test the detector in measuring photons and to calibrate the GUI. To test the detector's response to

neutrons, a sealed 2.0 Ci source of Plutonium-Beryllium (Pu-Be) was used, which emits neutrons and photons, simultaneously, through an (α ,n) reaction.

All of the sources mentioned above, are all kept within the Nuclear Measurements Laboratory located in the College of Engineering at the University of Nevada, Las Vegas. In addition to these sources, there are other sources that reside within the laboratory, however they are relatively small sources of radiation. The main source of radioactivity in the laboratory is the Pu-Be source, and is the focal point of the radiation measurements.

The Nuclear Measurements Laboratory is a reinforced concrete vault that is approximately 20 feet by 13 feet, and stands at a height of approximately 16 feet. The laboratory is used primarily for the radiation measurement of materials that are exposed to the Pu-Be source that is kept in the laboratory. The source carries a radioactivity of 2.0 Curies (Ci) and sits in the center of a 55 gallon drum, shown in Figure 27.



Figure 27 - Plutonium-Beryllium (Pu-Be) Source in the Nuclear Measurements Laboratory at UNLV

The Pu-Be source is always kept in the corner of the laboratory so that the two walls of concrete act as a neutron shield for the neutrons that the source emits. Likewise, on a third side of the source lays a thick sheet of high density polyethylene which is used to shield the test operator from over-exposure to neutron radioactivity.

Inside the 55-gallon drum is a homogenous mixture of PuO_2 and BeO powder, which acts as the source, the plutonium material is Plutonium-239 (^{239}Pu). The drum has a diameter of approximately two feet and has a height of approximately three feet. The source, itself, is approximately two inches in diameter and two inches in height. Under normal conditions, known as the “closed” position, the source sits at a position of approximately $\frac{2}{3}$ of the drum’s height, below the top surface of the drum, inside of an access port. Completely surrounding the source, inside the walls of the drum, is a layer of paraffin that is used to shield much of the radiation from the users. This setup is shown in a schematic in Figure 28.

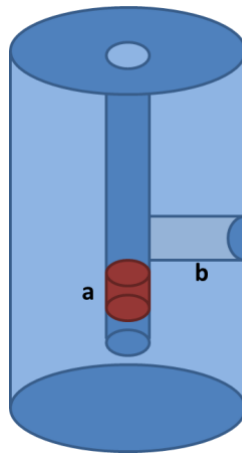


Figure 28 - Pu-Be Source Schematic Showing the (A) Pu-Be Source in the "Closed" Position, and the (B) Neutron Beam Port

In Figure 28, the area inside the drum surrounding (a) and (b) is filled with the layer of paraffin. The space labelled (b) is known as the neutron beam port, and is also shown in Figure 27. This port, in the “closed” position, is plugged with a rod of polyethylene that is designed to shield neutrons inside the drum.

When measurements are taking place, the source is raised into the “open” position, by means of the control rod. By locking the control rod in the “open” position the source (a) shown in Figure 28 is raised so that it is now in-line with the neutron beam port. Upon removing the polyethylene plug from the port, a beam of fast neutrons is formed and exits the drum with a flux of approximately 10^5 neutrons per second. This beam is un-moderated by any material and is used in the radiation measurements of fast neutrons. The average neutron energy is approximately 4.5 MeV, with the largest neutron energy value at approximately 3.7 MeV. The photons emitted from the source are very energetic, measuring to be approximately 4.43 MeV.

3.4 Experimental Setup

For the single scintillator detector experiments, detecting neutrons and photons then performing Pulse Shape Discrimination analysis on the measurements to differentiate the detections into one of two categories, the plastic scintillator system was set in line with the fast neutron beam, approximately one foot from the wall of the drum containing the Pu-Be source. This setup is shown in Figure 29.



Figure 29 - Single Detector Experiment with Pu-Be Source

For the task of performing time-correlation analysis on multiplicity measurements, the ^{60}Co source was used due to its decay scheme shown in Figure 30. Even though the activity of this source is small ($<0.1\text{-}\mu\text{Ci}$ factoring in the decay of the isotope), emits two photons of almost equal energies. This is shown by the decay scheme of ^{60}Co , shown in Figure 30.

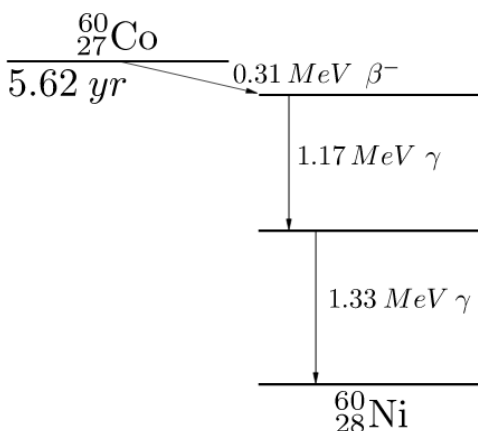


Figure 30 - Decay Scheme of ^{60}Co [60]

As Figure 30 would suggest, the two detectors of the array will be seeing two distinctly energetic photons, one at 1.17 MeV and the other at 1.33 MeV. The two photons emitted through the decay of ^{60}Co to ^{60}Ni , are released within 10^{-12} seconds of one another, with the emission of the 1.17 MeV photon first. This photon is emitted at any angle, completely unrestricted. However, the emission of the 1.33 MeV photon is emitted at an angle that must satisfy the conservation of momentum. If the detectors are properly placed, they should see both particles emitted from the source, and the “sandwiching” of the ^{60}Co source by the two detectors (Figure 31) represents the largest probability of multiple coincidence events to be detected. The source itself measures 2.0 inches in diameter and 0.115 inches in thickness, so the two inch face of the detector easily encompasses the entirety of the ^{60}Co source. Therefore, the chances that a photon emission from the ^{60}Co source is missed by the detector are small. This experimental setup is shown in Figure 31.

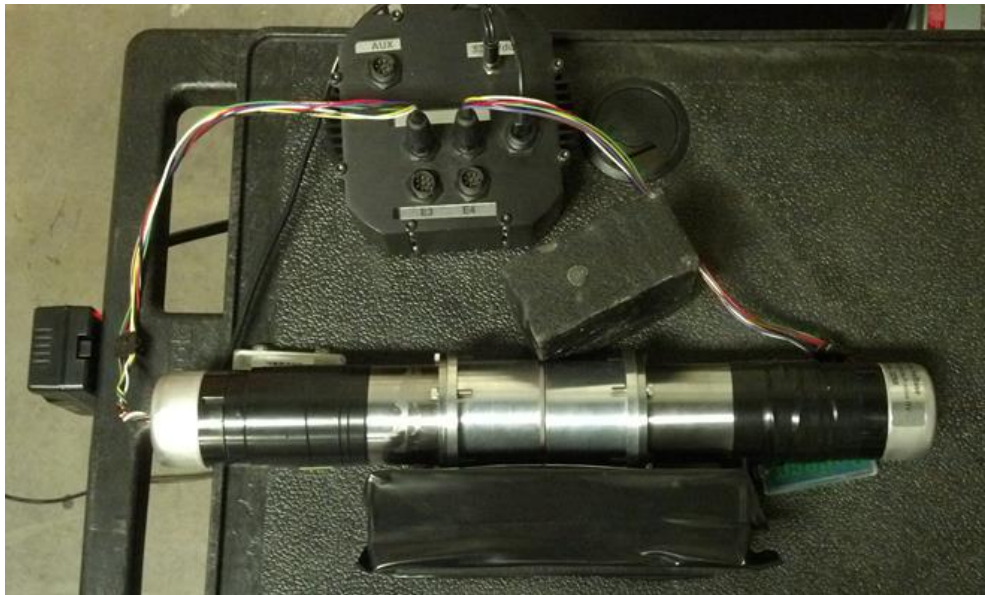


Figure 31 - Time Correlated Measurement using Two Detectors and ^{60}Co Source

As for the task of modeling a multiplicity experiment in MCNP to determine how much more effective the scintillator detector is as compared to a Helium-3 detector system, the simulation of a four array detector system that performs time correlation measurements of a fission source was created using MCNPX as the modeling application. The simulated model was built following the schematic shown in Figure 32, which follows the schematic of the four detector multiplicity experiment discussed in [22].

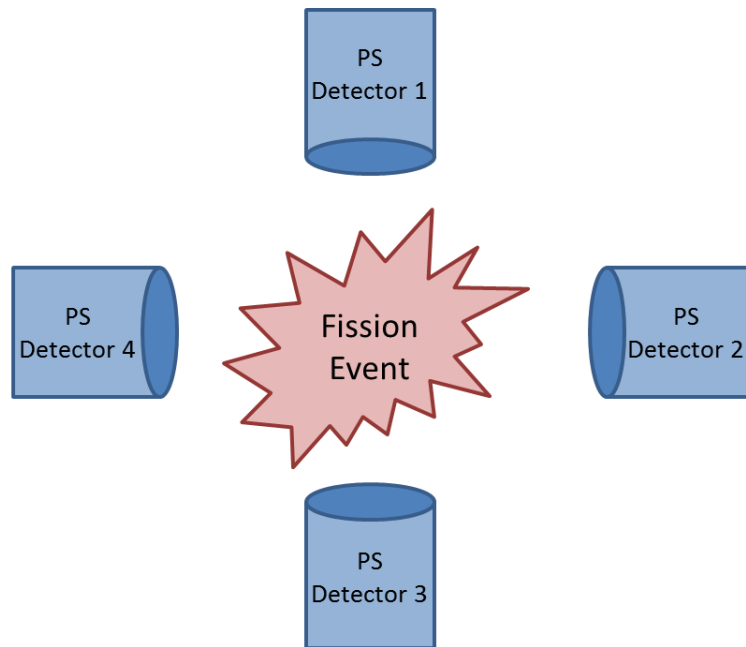


Figure 32 - Schematic of the Four Detector Array Setup for Multiplicity Modeling

CHAPTER 4

RESULTS AND DISCUSSION

4.1 Neutron Measurements using Single Detector System

4.1.1 Calibration of Single Detector Using ^{60}Co Source

The EJ-299-33A scintillator detector was constructed following the techniques discussed in Chapter 3. With the detector constructed in a light tight manner, tests were done using a small source of ^{60}Co , with a measured activity of 0.1 μCi recorded on November 22, 2011, $A(t=0)$. The current activity, $A(t)$, of the ^{60}Co source, approximately X years later, can be determined following the radioactive decay equation shown in Eq. 23, where t is the total elapsed time, in seconds, since the original source measurement was taken, and λ is the decay constant of ^{60}Co .

$$A(t) = A(t = 0)e^{-\lambda t} \quad (\text{Eq. 23})$$

Using this equation, the current activity of the source of ^{60}Co is expected to be approximately 0.0743 μCi . This is important to determine as the activity of the source plays a direct roll on the outcome of the photon spectrometry of the ^{60}Co source.

The isotope ^{60}Co makes for a great calibration source due to the energy of the photons that are emitted from ^{60}Co as a result of its radioactive decay. It releases two energetic photons, 1,332.5 keV and 1,172.5 keV, which can be used as a means to calibrate a detector system because of its known photon energy levels. In order to adequately calibrate the EJ-299-33A plastic scintillator system, a source of ^{60}Co was selected.

In Figure 33, the experimental setup is shown for the single EJ-299-33A scintillator detector, sitting directly on-top of the calibration source of ^{60}Co , which is shown in Figure 34. The measurement was conducted in the same room which houses the PuBe source, although the measurement was done in a different part of the lab. However, to increase the probability that the detector was only reading photon emissions from the ^{60}Co source, 2 in thick bricks of lead were used to isolate the measurement from other radiation as the misdetection of neutrons from the neutron source could cause error to be introduced to the measurements which leads to the idea of isolating the experiment from other sources.



Figure 33 - Calibration of Neutron Scintillator Detector



Figure 34 - ^{60}Co Source used to Calibrate EJ-299-33A Detector System

Using the GUI developed by Bridgeport Instruments (BPI), to act as a means to communicate with the eMorpho data acquisition unit a calibration measurement of the ^{60}Co source was conducted. The layout of the GUI is displayed in Figure 35, which loads on startup with predefined input parameters of a Quality Assurance test conducted by BPI.

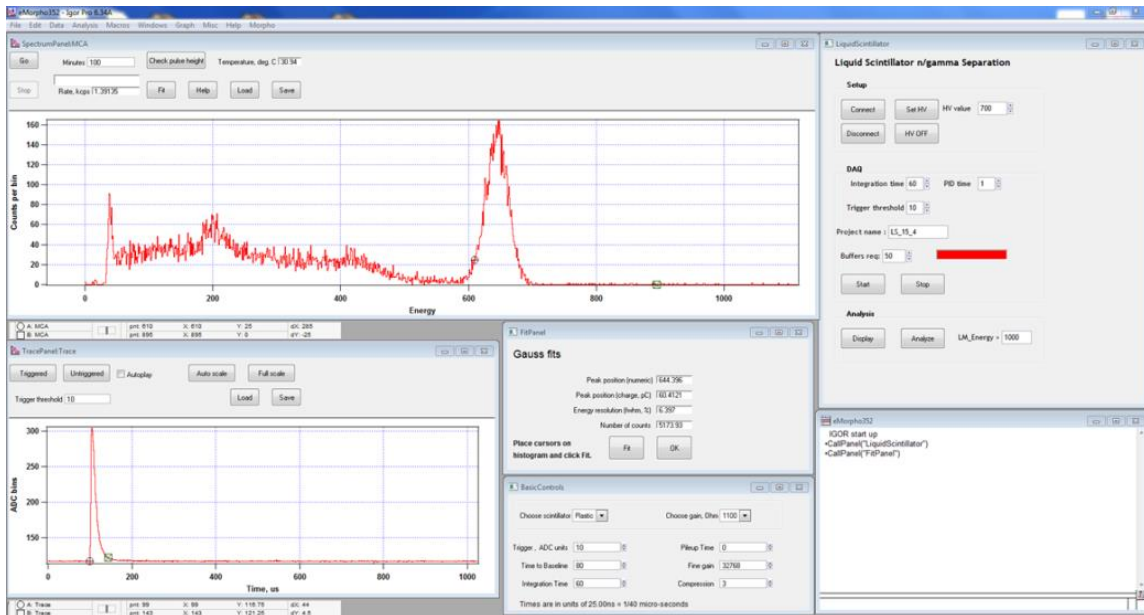


Figure 35 - eMorpho GUI

In the GUI, the user defines a series of inputs that are dependent on the detector system which will be used for the measurement of radioactive sources. After establishing a connection with the detector system, the eMorpho is prepared to receive the defining characteristics of the detector system, located in the “Basic Controls” (Figure 36) section of the GUI.

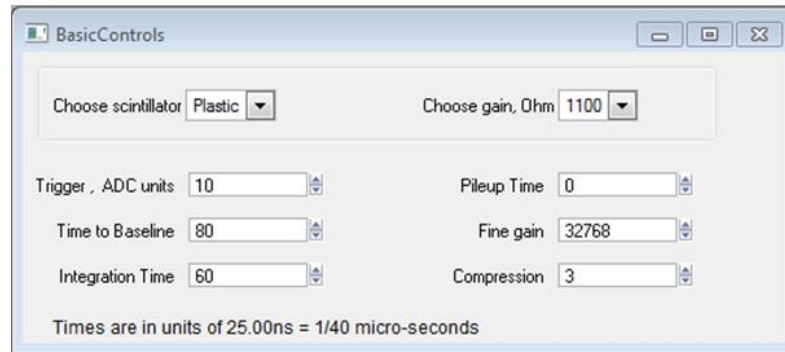


Figure 36 - Default Basic Controls Panel in the eMorpho GUI

Table 4 shows each of the entry fields from the Basic Controls panel in Figure 36 and a short description of its effect on the DAQ and FPGA hardware within the eMorpho.

Table 4 – Inputs of eMorpho GUI [61]

INPUT FIELD	DESCRIPTION
Choose Scintillator	- Allows user to select a detector medium from a list of predefined materials
Choose Gain, Ohm	- Allows user to define current-to-voltage converter from five selectable gains (100 to 10,100)
Trigger, ADC Units	- Allows user to define the base pulse requirement for the pulse to be considered a measurement, triggering the detection
Time To Baseline, ADC Units	- Allows the user to instruct the eMorpho to wait after a trigger before a new trigger can be recorded (a.k.a Trigger Dead Time)
Integration Time, ADC Units	- Allows user to define integration window used for determining the pulse energy and PID value
Pileup Time, ADC Units	- Allows the user to instruct the eMorpho to recognize pile-up pulses, rejecting pile ups if desired.
Fine Gain	- Allows user to finely tune the detector for accurate measurement, using an adjustable fine gain (32,768 = unity gain)
Compression Factor	- Used to fit the energy histogram into the allowable 4,096 energy bins of the FPGA

In addition to establishing the basic controls for the DAQ system, the user can define the High Voltage (HV) gain to the eMorpho DAQ from the “Set HV” panel shown in Figure 37. After setting the high voltage, and defining a runtime, the DAQ is ready to begin collecting pulse information.

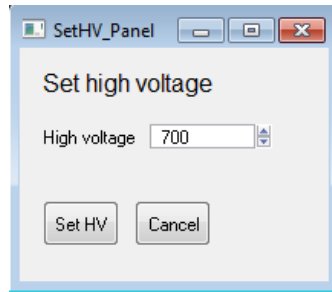


Figure 37 –HV Setup Panel

Other important windows to note from Figure 35 are the Histogram and Trace Windows, located in the top right and bottom left of the GUI in Figure 31. The histogram shows the steady accumulation of detected pulses as the project runs. In addition it allows for the establishment of a Gaussian Fit curve to isolate key characteristics of the energy spectrum. As for the Trace window, each triggered pulse is displayed in the Trace window of the GUI. It allows for the optical readout of the PMT Pinouts. It is also the starting point for the PSD Analysis with the implementation of the PSD program shown as the top right window in Figure 35.

This program allows the user to define an integration time and a PID Time value which are used to analyze pulses for particle identification using PSD techniques. The program analyzes each pulse by measuring their Partial Integration Time (PIT) and comparing it to the Total Integration Time (IT) of the same pulse. This technique is

shown in Figure 38. Each trigger in the DAQ is caused by a measurement pulse of a particle. The total integral of the pulse, i.e. the total time under the curve, represents the Total Integration Time. The program then calculates the Partial Integration Time by only measuring a portion of the pulse, which is measured based on the variable input entered by the user (PID time).

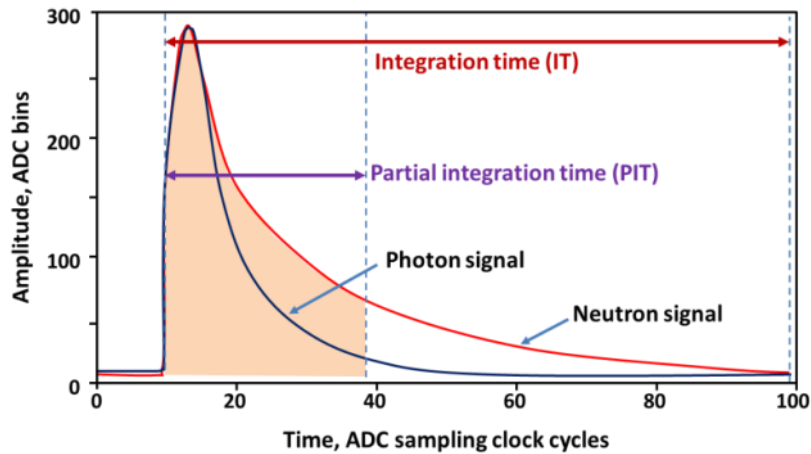


Figure 38 - Pulse Shape Discrimination Scheme Showing Differences in Photon and Neutron Trace Signals [12]

Neutrons and photons have two distinct pulse shapes when detected by the scintillation material. Because of this, the exploitation of their unique shapes allows for the separation of each particle type. For example, photons interact with the scintillation material and cause a burst of scintillation that decays, much faster than that of the neutron-induced scintillation. Thus, the PIT of the neutron results in a larger value than that of the photon.

By taking the ratio of the calculated PIT value and the IT value of each pulse, the resulting term is then known as the PID value or PID. It is important that this is

not to be confused with the user defined input for the PID time value which is used in determining the PIT of each pulse. Because the PID is larger for neutron pulses, neutrons and photons can be adequately separated based on their PID values.

The output of this program displays the information in three graphs: 1) a standard Counts vs Energy Histogram, 2) a distribution curve of particles, and 3) a plot of the separation of photons from neutrons based on their calculated PID values.

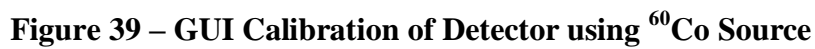
For the calibration of the detector using the ^{60}Co calibration source, and for all future measurements, the eMorpho GUI basic controls inputs were defined following the information displayed in Table 5. The control parameters were determined through trial and error, with time taken to determine the most efficient setting for each parameter. After initial measurements of the ^{60}Co source, the resulting GUI is shown in Figure 39.

Table 5 –Inputs of eMorpho GUI for ^{60}Co Measurements

INPUT FIELD	Input Value
Choose Scintillator	- Plastic
Choose Gain, Ohm	- 1,100
Trigger, ADC Units	- 10
Time To Baseline, ADC Units	- 150
Integration Time, ADC Units	- 100
Pileup Time, ADC Units	- 100
Fine Gain	- 29,500
Compression Factor	- 2

The scintillator was chosen to be “Plastic” since the EJ-299-33A scintillator is composed of plastic materials. For the gain, the 1,100 Ω transimpedance current-to-voltage converter circuit allowed for the most accurate calibration of the GUI. The Trigger was left at 10 ADC units so that more pulses would cause triggers within the

FPGA. The Time to Baseline was chosen to be a time that is high so that each triggered pulse is separate from one another, and not resulting in the creation of a double pulse. The Integration Time was selected as 100 ADC Units as it produced the best measurement results when coupled to the longer Time to Baseline values, and likewise the Pileup was set to equal to Integration Time so that Pileup Rejection is turned off (not necessary for this measurement environment). The Compression Factor was left as the default value, 2, because of sufficient compression of the Histogram. The resulting GUI output, which ran for a data collection time of 20 minutes, is shown in Figure 39



In Figure 39, the GUI recorded the Energy Histogram of each pulse, taken at time intervals of every 1.875 μs , which is determined by the conversion of ADC Units to clock cycles following:

$$Time\ to\ Baseline\ [ADC\ Units] * \frac{12.5ns}{ADC\ Unit} = Time\ [ns] * \frac{1\ \mu s}{1000\ ns} = Time\ [\mu s] \quad (\text{Eq. 24})$$

The Energy Histogram, shown in Figure 40, displays the number of measured counts per energy bin. In Figure 40, the energy bins have been calibrated adequately by the adjustment of the Fine Gain, which was lowered to 29,500 rather than the unity gain value of 32,768. The second energy peak in the histogram is caused by the release of the 1,332.5 keV and 1,172.5 keV photons from the ^{60}Co .

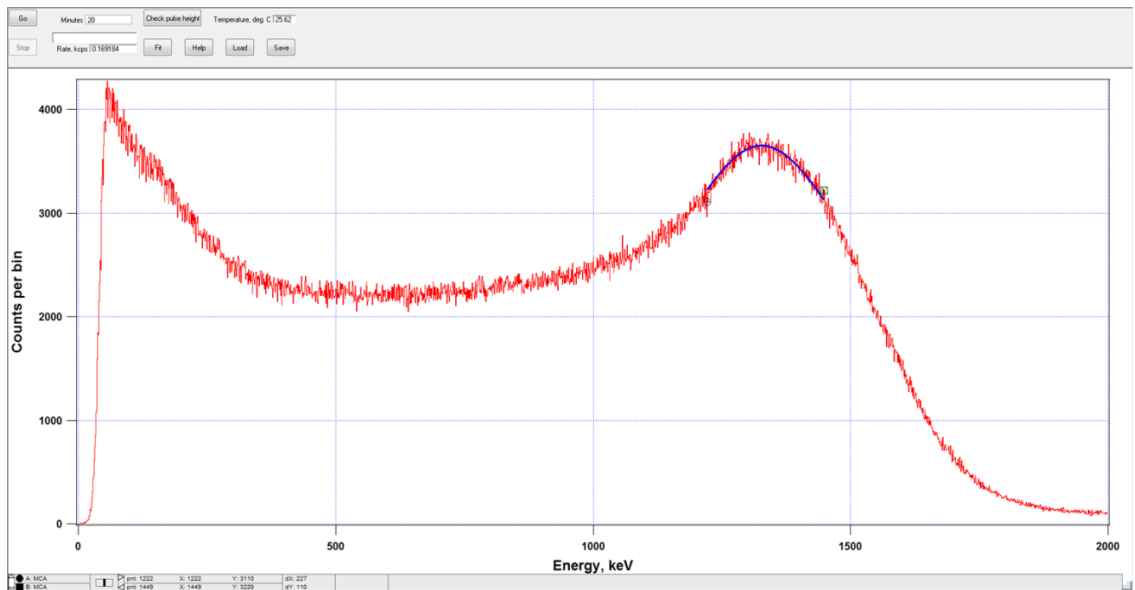


Figure 40 – Energy Histogram of ^{60}Co Source with a Gaussian Fit

A Gaussian Fit curve was added to the histogram to determine the position of the energy peak. The resulting peak location was then used to experimentally determine the

value required for the Fine Gain such that the Histogram would be calibrated for measurement.

4.1.2 Measurement of ^{137}Cs

To confirm the eMorpho GUI and DAQ is calibrated correctly, a test was conducted using a 0.1 μCi source of ^{137}Cs . Similar to ^{60}Co , ^{137}Cs releases pure photon radiation, with the emitted photons carrying energy of approximately 662 keV. The resulting spectrometry histogram for the 0.1 μCi source of ^{137}Cs is shown in Figure 41. As can be seen, the photon released from the ^{137}Cs source carrying energy of 662 keV can clearly be seen and is in the right position for the spectrum expected when using ^{137}Cs .

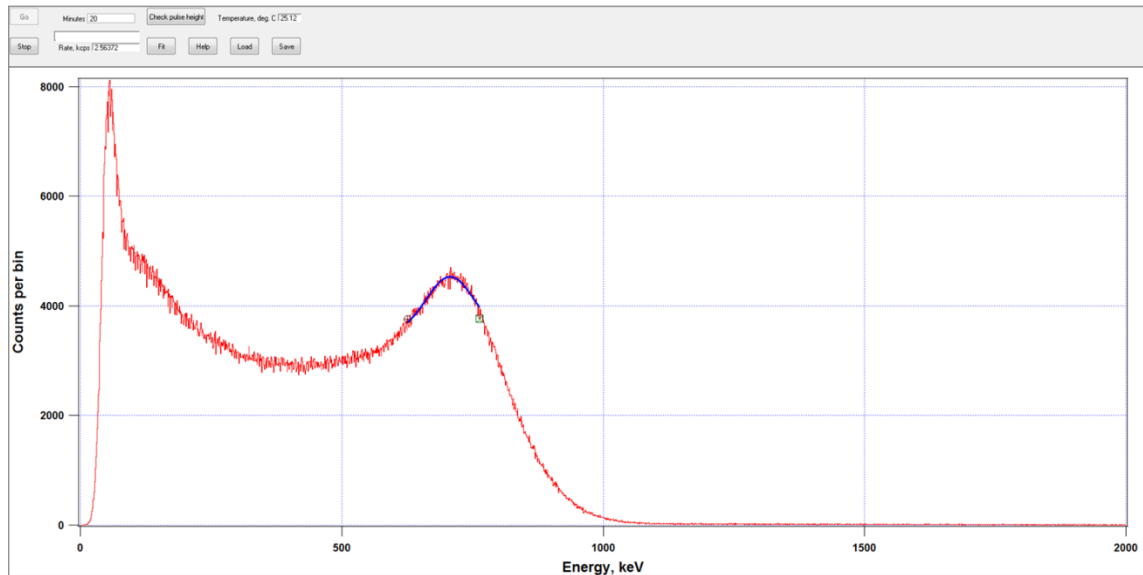


Figure 41 – Energy Histogram of ^{137}Cs Source with a Gaussian Fit

4.1.3 Analysis of Pulses using Pulse Shape Discrimination Technique

During measurements of the Pu-Be neutron source using the EJ-299 Scintillator Detector system, the Pulse Shape Discrimination program was initiated. Once the PIT is known for the pulse, the program executes the analysis to determine the pulse's Total Integration Time (IT). Next, the program takes a ratio of the PIT to the IT following the equation:

$$\frac{PIT}{IT} = PID \text{ Value} \quad (\text{Eq. 25})$$

It is important to note that the PID Value is not the user defined PID Time value. The program is then instructed to perform this process on 250 buffers, where each buffer represents full list mode storage, of 340 events. This gives an adequate collection of data to reliably analyze and process for radiation separation. The following paragraphs delve into the result of the neutron/ gamma measurement from the Pu-Be source.

Each pulse triggered in the detector system was analyzed for its time properties. Figure 42 and 43 show the trace window generated during the measurements. Evaluating the traces with the naked eye, one is hard pressed to notice the slight differences in the pulse's time properties, namely the decay of the pulse. However, looking closely one is able to notice that on the decay of each trace, the tails differ slightly. In Figure 42, the decay of the pulse returns rapidly to its original starting position of approximately 125 ADC Bins then remains there for the remainder of the window, suggesting the pulse was caused by the detection of a photon. Conversely, the pulse shown in Figure 43 shows a rapid decay of the pulse, however as it gets closer to its original starting position of 125

ADC Bins, the pulse hovers at 130 to 145 ADC bins, before slowly decaying back to its original position, which suggests that the pulse was caused by a neutron.

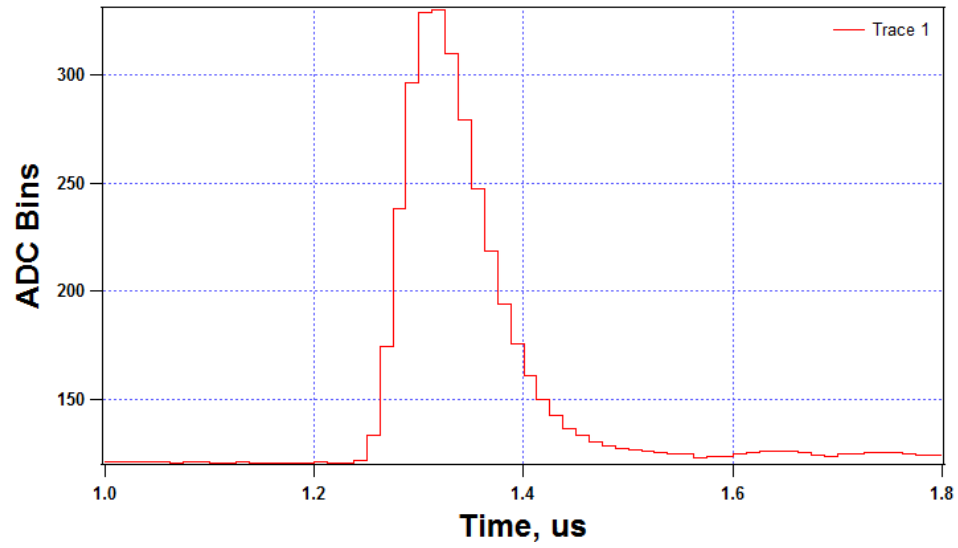


Figure 42 – PMT Anode Pulse Produced by a Photon

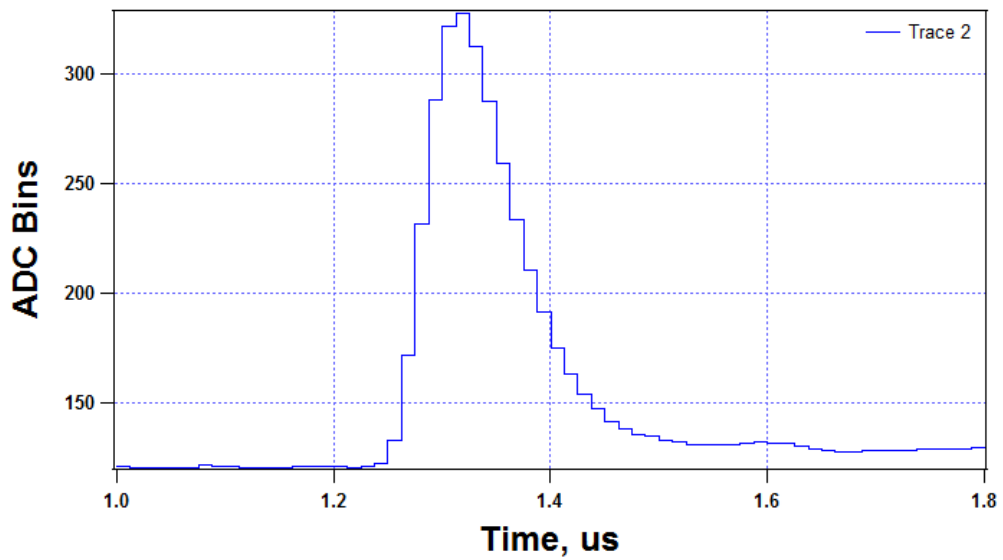


Figure 43 – PMT Anode Pulse Produced by a Neutron

To show the differences between the two pulses, the data was concatenated to create the graph shown in Figure 44. Here, the difference in the decays of the pulses becomes a little clearer. This slight difference in pulse shape is enough for the Pulse Shape Discrimination software to exploit and separate these two pulses into their respective radiation types.

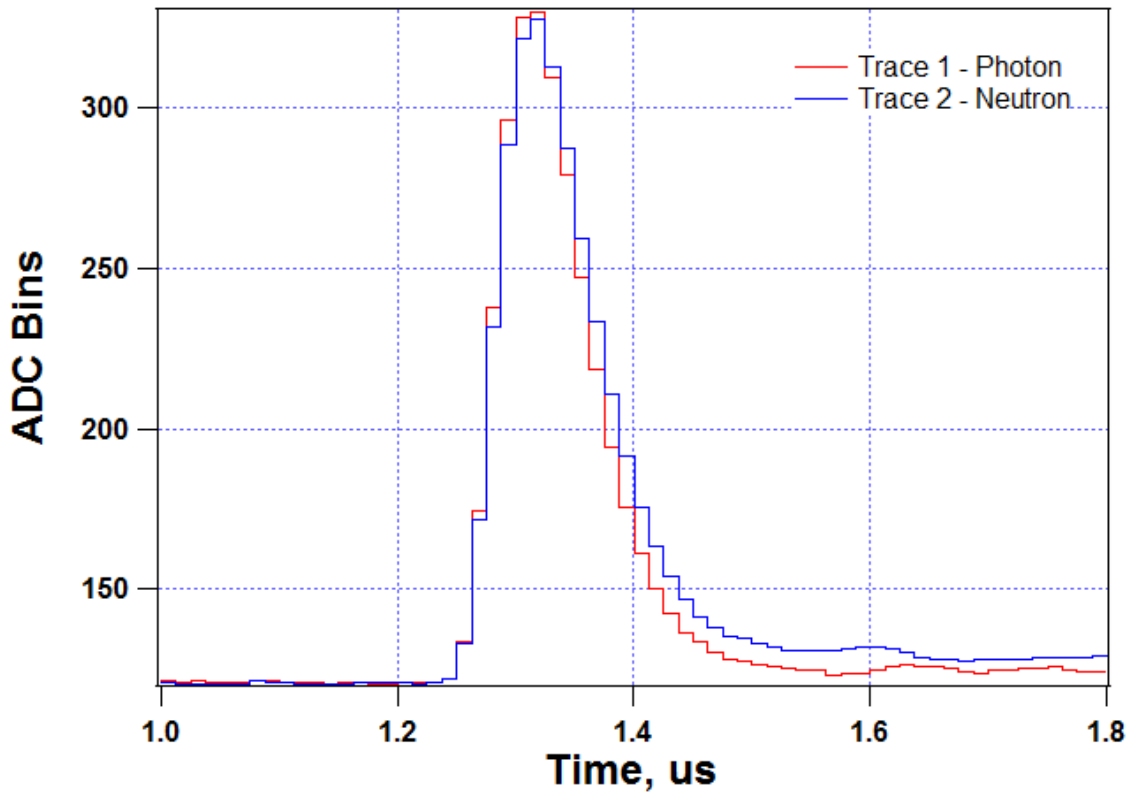


Figure 44 –Photon and Neutron Traces from Pu-Be Source

This analysis process was repeated 340 times for each of the 250 buffers. The results of each triggered events are shown in Figures 40 and 41. In Figure 45, a plot was created showing the scatter of the radiation detected by the scintillator detector. Each

pulse's PID Value is plotted against the calculated energy, in keV electron equivalent (keVee), of that pulse.

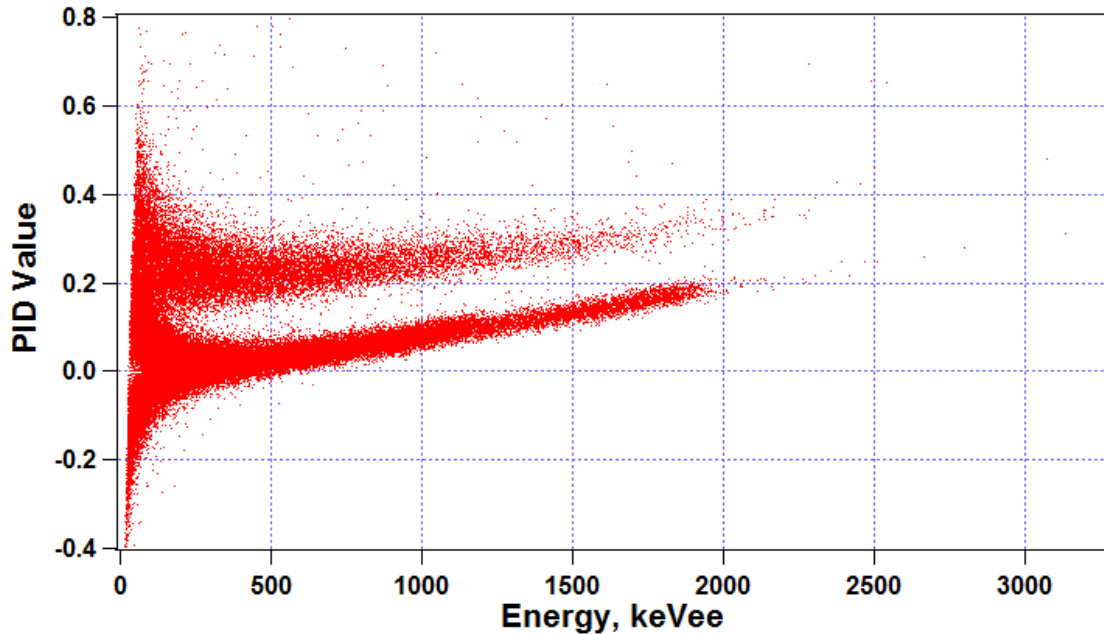


Figure 45 – PSD Analysis Results of Pu-Be Neutron/ Gamma Source

In Figure 45, it is shown that there is a very clear grouping of two types of PID Values, one that is distributed about 0.18 PID Value and the other distributed about 0.39 PID Value. The small difference, shown in Figure 39, is enough the PSD Technique to separate pulses. In Figure 45, the grouping at 0.39 represents the emitted neutrons from the Pu-Be source because the PIT of the neutron pulse is slightly larger than that of the photon pulse. As a result, PID values above 0.24 are classified as neutrons, while the lower PID Values are classified as photons.

It is important to note that the clear separation of neutron pulses from photon pulses is largely dependent on the user defined variable, PID Time. The reason for this is

that if this PID Time is inputted with too low of a value then the results of Figure 45 would become much more concatenated, meaning that the two groupings would mix, and no clear separation of radiation types would be able to be seen. Conversely, if the PID Time input value is too high, then photons would cross the separation threshold and be falsely counted as neutrons. For this application, the ideal PID Time value was 18 units. The lower threshold of this input was determined experimentally to be 15 units and the upper threshold was found to be 20 units.

To clearly show the distribution of the photon and neutron signals, the second output of the PSD program groups the particles recorded in Figure 45 and delegates them into two very clear distributions of PID Values, shown in Figure 46. In this figure, the larger distribution represents the photon group of traces, which centers the distribution on approximately 0.5 to 0.8 in PID Value, which collaborates with the information shown in Figure 40. Likewise, the second distribution shown in Figure 46 represents the grouping of neutron PID Values, centered at approximately 0.25 in PID Value.

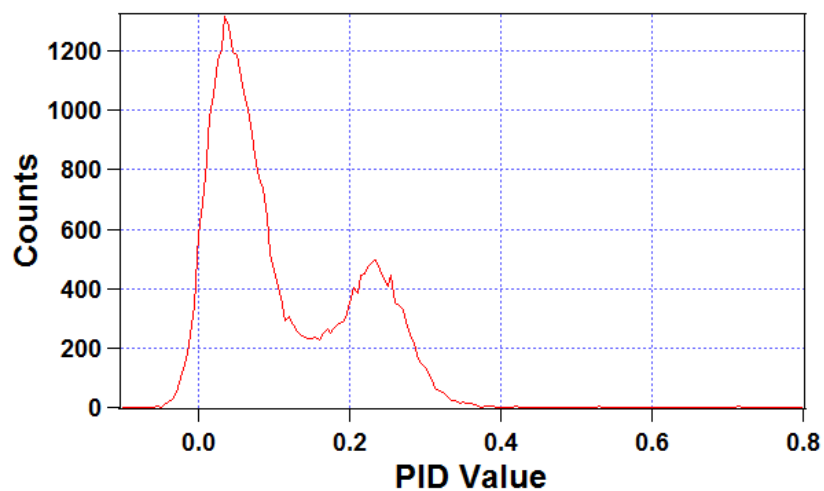


Figure 46 – Pu-Be PSD Distributions Based on Radiation’s PID Values

To confirm the outputs of the of the PSD program, the program was ran with the ^{60}Co source. Figures 47 and 48 show the resulting outputs of the PSD program for the ^{60}Co measurement.

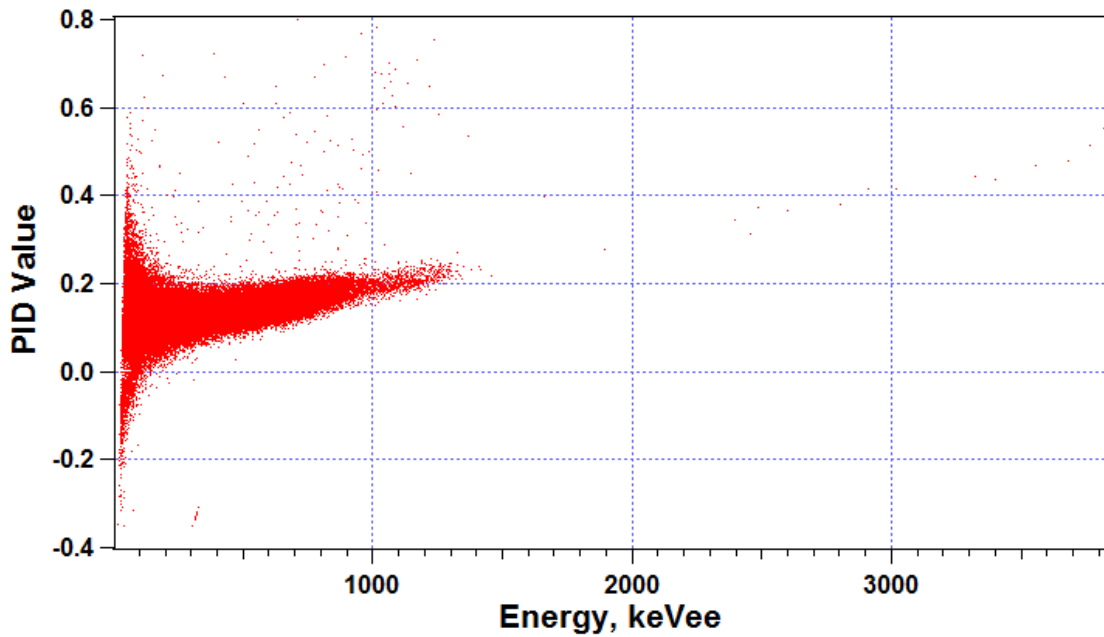


Figure 47 –PSD Results from ^{60}Co Showing no Grouping of Neutrons

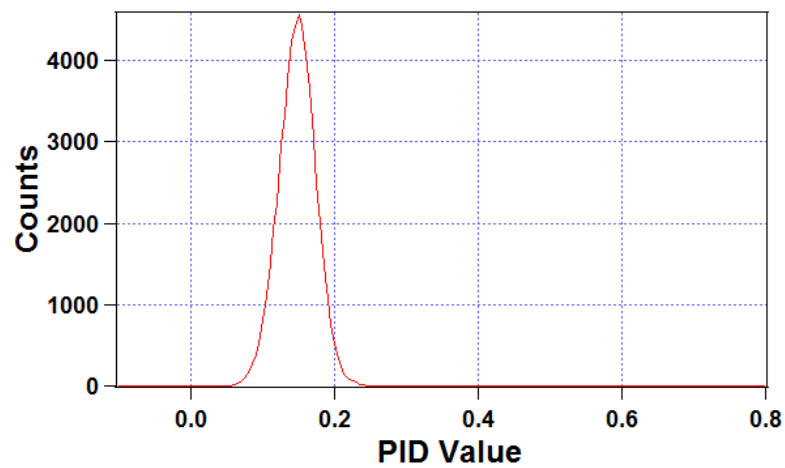


Figure 48 – ^{60}Co PSD Distribution Showing Pure Photon Distribution

As can be seen in Figures 47 and 48, the results of the PSD program using a ^{60}Co as the radiation source, resulted exactly as predicted. In Figure 47, the PSD Technique revealed that there was only one grouping of similar PID Values. The neutron group that was seen in Figure 45 is not present. Figure 48 supports this claim showing only a clear group of radiation with a distribution of PID Values that centered on 0.18 PID Value. These results confirm the accuracy of the outputs from the PSD Program.

4.2 Time Correlation Measurements using Two Detector System

To perform the Multiplicity Measurements, the qMorpho was used to read the pulses off two EJ-399-33A Plastic Scintillator Detectors and analyze them on the same time base. First, it is necessary to determine the user defined inputs for the qMorpho system. For several of the User Defined Input Fields, the descriptions from Table 4 hold true. However, new input values have been created for use with the qMorpho, which are discussed in Table 6. It is important to note how qMorpho counts its channels. The Detector attached to E1 is recorded as Ch. 0 within the GUI. Likewise E2, E3, and E4 correlate to Ch. 1, Ch. 2, and Ch. 3, respectively. Refer to Figure 20 for a visual.

Several of the parameters are consistent with the setting for eMorpho's GUI. Such examples include Integration Time, Fine Gain, and Trigger Threshold. Some parameters were renamed (i.e. Trigger Dead Time), and others were redefined to accommodate the complexity of the qMorpho system. An example of this is seen in the Gain Resistor Pattern which defines the resistance of each ADC channel. In eMorpho, the user defined the resistance to be 430 Ω , 1,100 Ω , etc. However, in qMorpho, more resistor patterns are available for the user to define. The GUI for qMorpho now rewrites each resistor pattern as a gate value. Different gate values lead to different combinations of resistor patterns

which lead to the use of different transimpedances for the qMorpho DAQ. To stay consistent with the eMorpho, the gate value for a resistor pattern for 1,100 Ω of transimpedance was used for all qMorpho measurements.

Table 6 – Input Values for qMorpho System

Input Field	Channel 0	Channel 1	Descriptor
Trigger Threshold	10	10	Required Pulse Height to Trigger Detection
Integration Time	100	100	Used to Determine Total Integration Time and Energy
Trigger Dead Time	150	150	a.k.a. Time to Baseline
Pile Up Rejection	100	100	Set Equal To Integration Time to turn off
Pulse Shape Analysis	18	18	PID Time
Gain Resistor Pattern	2	2	Gain Pattern of 2 = 1,100 Ω
Energy Compression Factor	3	3	Used to Compress Energy Spectra into MCA Bins
Fine Gain	42500	52500	Used to Calibrate the Response
Energy Compression for PID	2	2	Used to Compress PID Value Results
List Mode Type	2	2	Collects Energy, Time, and PSD Words
Requested Runtime	50 Buffers	50 Buffers	1 Buffer = 340 Events
16-Bit Coincidence Mask	8	8	CM = 8 define hit pattern for Ch. 0 and Ch. 1
Coincidence Window Length			Allowable window for Coincidence to occur

To measure the time coincidence detection of radiation within the Plastic Scintillator, the ^{60}Co source was used. The reason for this is that ^{60}Co emits two photons of approximately equal energy in directions that are purely opposite of one another, refer to the decay scheme of ^{60}Co shown in Figure 30. Because of this feat, ^{60}Co can be used to perform gamma-gamma time coincidence measurements.

Figure 49 shows the triggered pulses of two radiation particles detected in the detectors on Ch. 0 and Ch. 1 of the qMorpho. The figure shows each pulse on its corresponding channel, but both channels show the same time base, which is measured in ADC Clock Cycles, where each clock cycle equals 12.5 ns in standard time measurements.

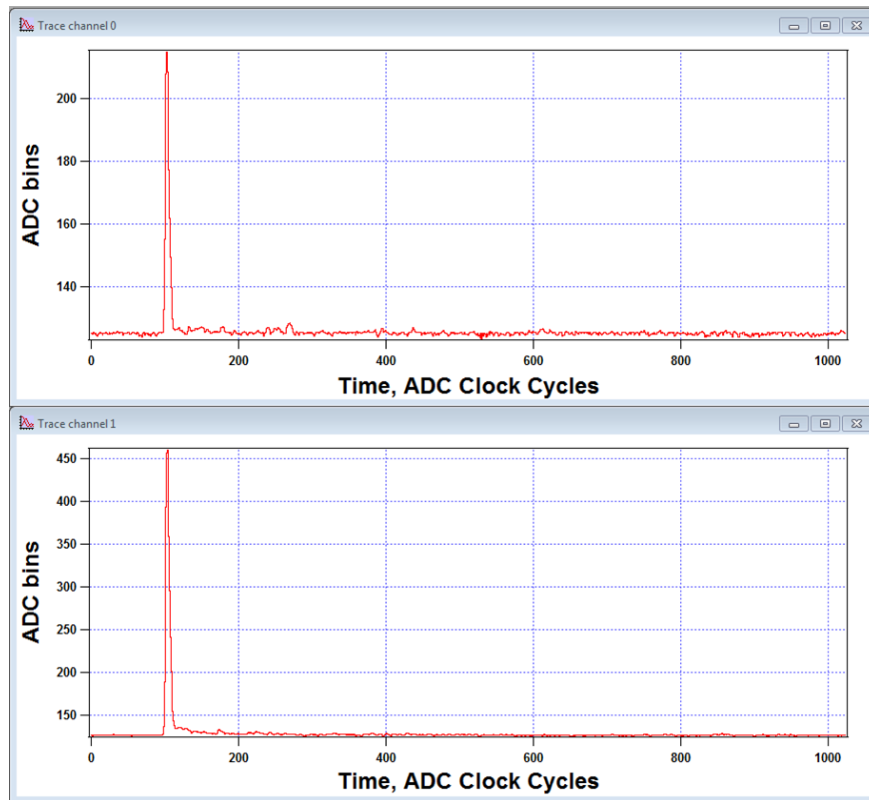


Figure 49 – qMorpho Time Coincidence Measurement of ^{60}Co on Two Channels

Although the two pulses measure in separate heights in terms of ADC Bins triggered, they both triggered within the detector at the same time. This is shown in Figure 50, where the two pulses are shown on the same X-Axis. The time base of each pulse was converted to standard time measurements of micro-seconds (μs), which is done by following Eq. 24.

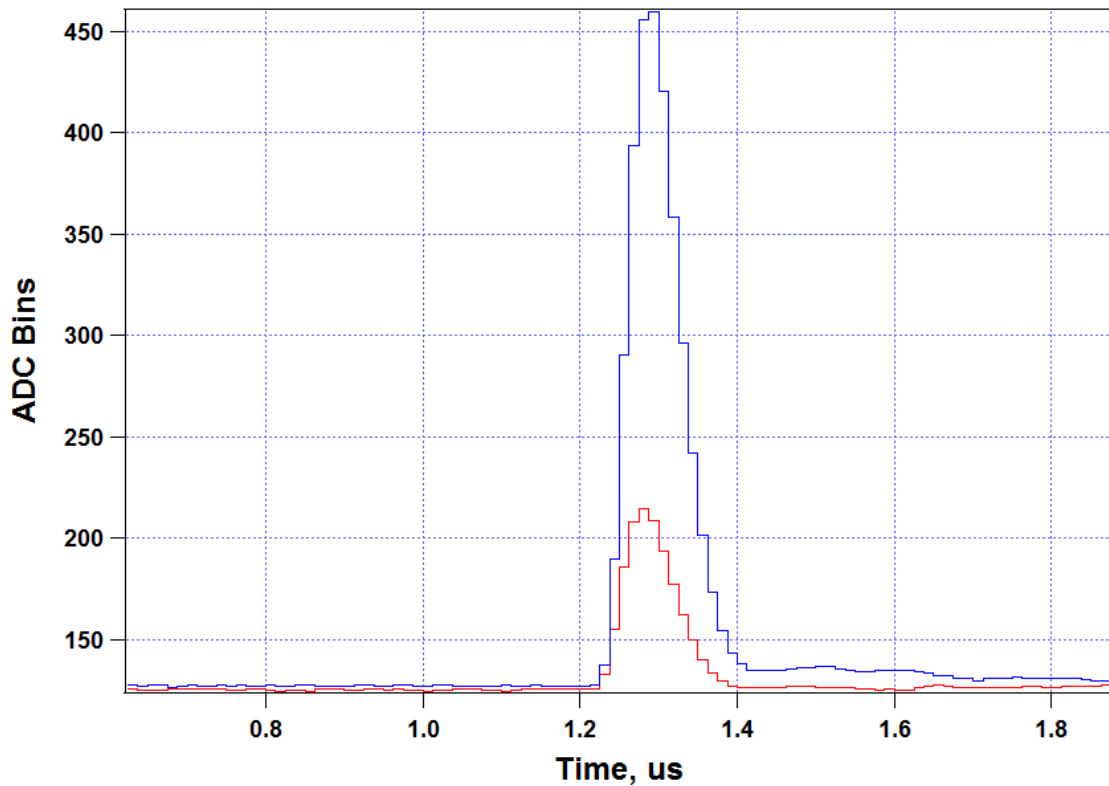


Figure 50 – Concatenated Pulses of qMorpho Measuring Two Detections of Radiation from ^{60}Co Source

From the pulses shown in Figure 50, both detection events were detected at the same time, which proves not only the time coincidence capability of the qMorpho system, but also the detection capabilities of the plastic scintillator detectors. In addition to this, Figure 50 provides another insight as to the length of the coincidence window that

could be defined for the time coincidence measurements. Since the pulses occur within approximately $0.05\ \mu\text{s}$ of each other (the beginning of their pulse curves), it is safe to assume that coincidence measurements can be collected with a coincidence window width of just $0.05\ \mu\text{s}$.

Figure 50 is just one coincidence event however. To obtain multiple coincidences, the qMorpho GUI was programed to obtain 50 buffers (where each buffer measures 340 events). The resulting measurements are shown in Figures 51 through 54. For these figure, the time coincidence window length was defined as 50 ADC Clock Cycles, which in standard time measurements is $625\ \text{ns}$ or $0.625\ \mu\text{s}$, well above the guess based on observational analysis.

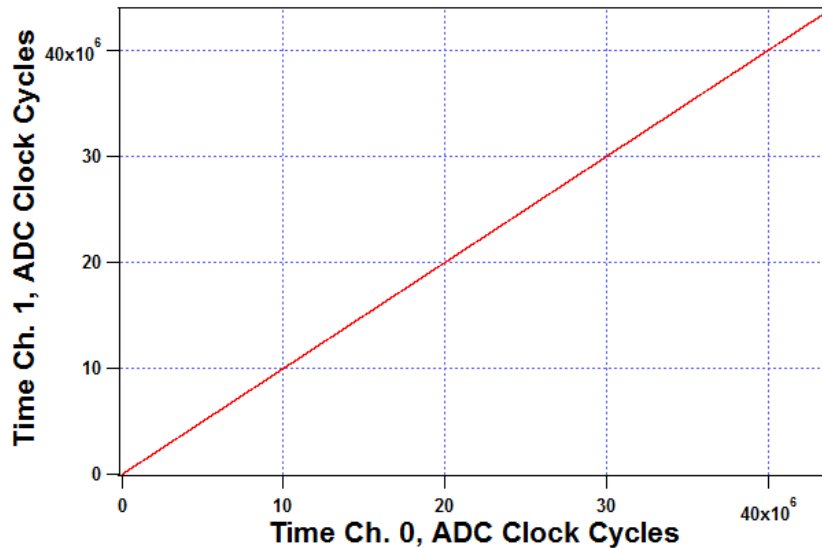


Figure 51 – Time Stamp Coincidence Between Two Channels of qMorpho

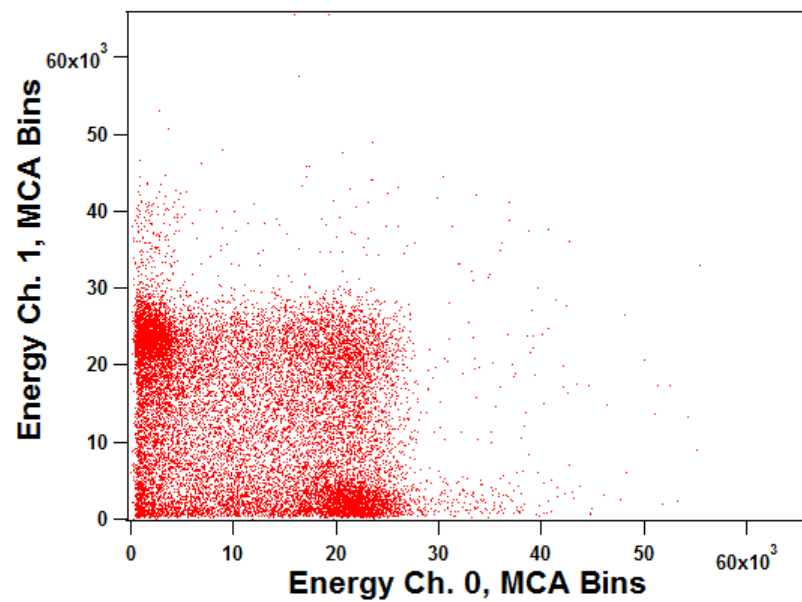


Figure 52 – Energy Coincidence Between Two Channels of qMorpho

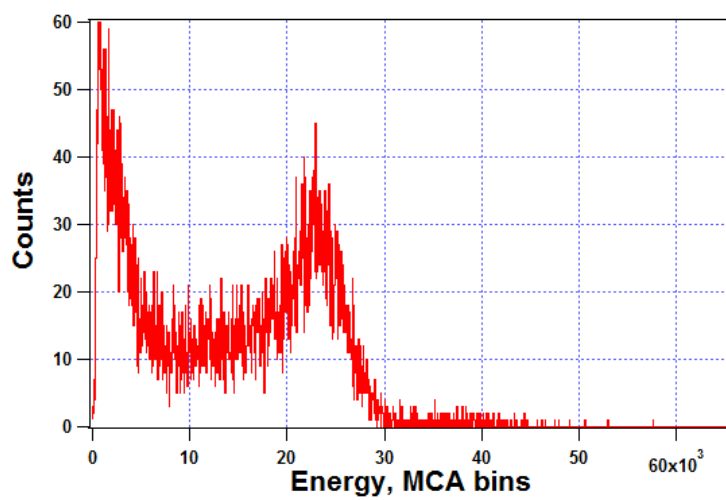


Figure 53 – Energy Spectra of ⁶⁰Co on Channel 0

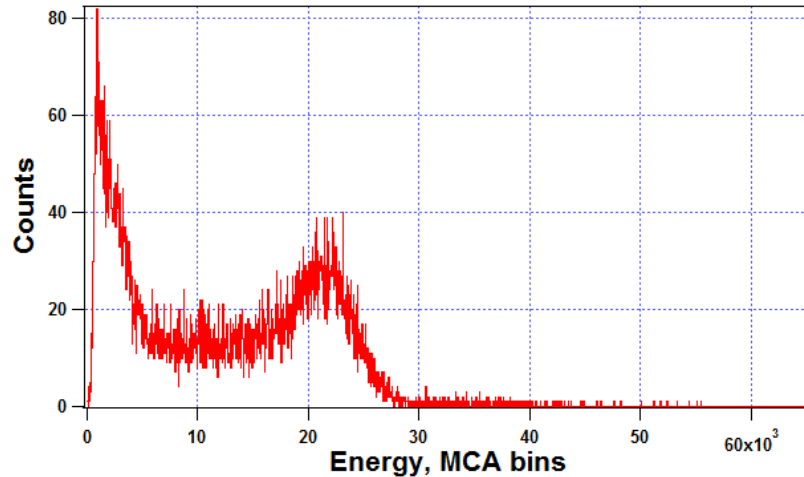


Figure 54 – Energy Spectra of ^{60}Co on Channel 1

Figure 51 shows a linear time coincidence measurement between Channels 0 and 1, which is to be expected when measuring from a source of ^{60}Co . In this figure, the time stamps for each coincidence event are recorded. Their corresponding energy points are then shown in Figure 52, which shows a scatter plot of coincidental energy values between both channels. In this figure, there are four distinct groupings of coincidental energies, one at low energies for both channels, one at high energies for Channel 0 and low energies for Channel 1, another at low energies for Channel 0 and high energies for Channel 1, and the last at high energies for both channels. The last grouping is not as strong as the other three due to the strength of the source energy spectrum which is measured for both Channels 0 and 1, displayed in Figures 53 and 54, respectively.

This test proves that time coincidence is viable with the detector system, but from the pulses shown in Figure 50, detection events are occurring within $0.05\ \mu\text{s}$ of one another. To test this observation, the coincidence window length for the qMorpho GUI

was shortened to just four ADC Clock Cycles, or 50 ns ($0.05\ \mu\text{s}$). The coincidence results are shown in Figures 55 and 56.

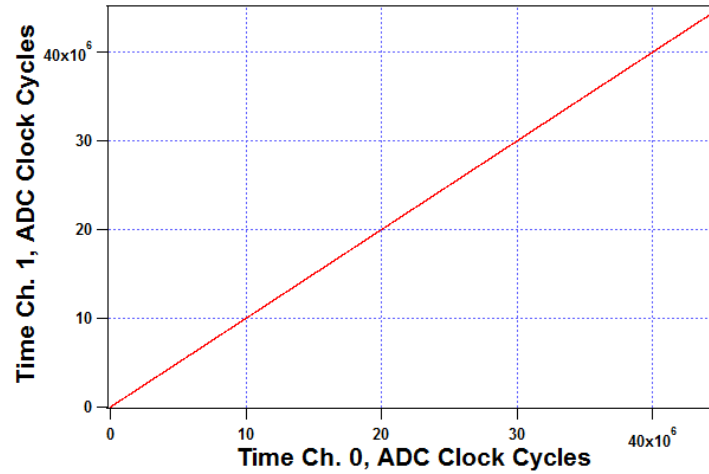


Figure 55 - Time Stamp Coincidence Between Two Channels of qMorpho with Coincidence Window at 4 ADC Clock Cycles

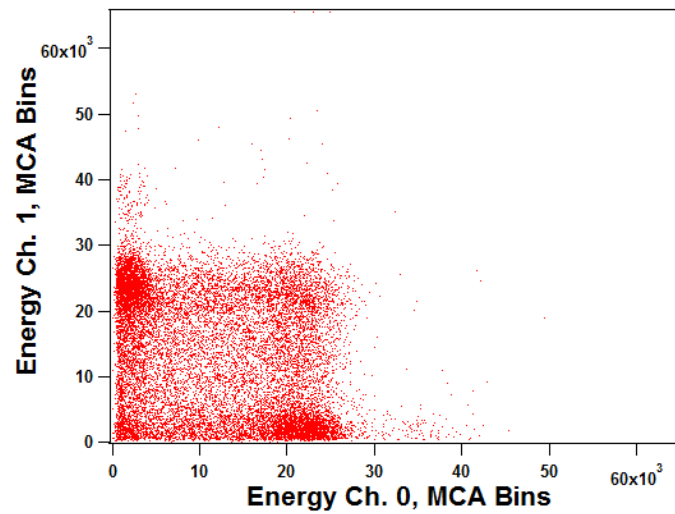


Figure 56 - Energy Coincidence Between Two Channels of qMorpho with Coincidence Window at 4 ADC Clock Cycles

Comparing Figures 55 and 56 with their respective counterparts in Figures 51 and 52, there are no significant differences when the window was changed, with the exception of the density of the coincidences increasing slightly between the two trials.

To conclude, the window length for the plastic scintillator detector system was reduced further, to only one ADC Clock Cycle (12.5 ns or 0.0125 μ s). The results are shown in Figures 57 and 58.

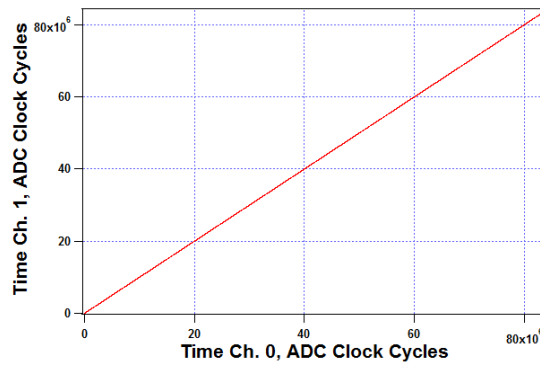


Figure 57 - Time Stamp Coincidence Between Two Channels of qMorpho with Coincidence Window at 1 ADC Clock Cycles

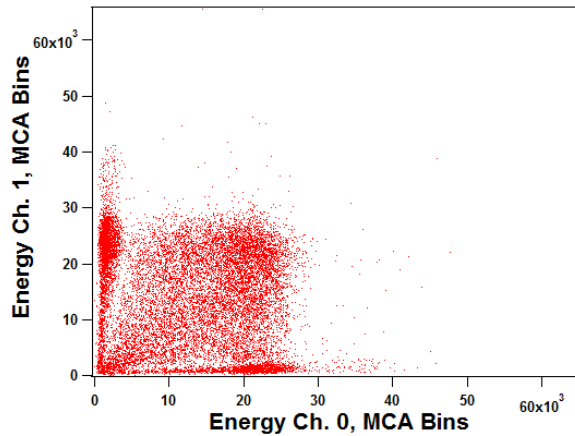


Figure 58 - Energy Coincidence Between Two Channels of qMorpho with Coincidence Window at 1 ADC Clock Cycles

Notice, when comparing Figure 83 to Figure 42 or Figure 56, the coincidence measurements at high energy values for the ^{60}Co spectra has drastically changed. The coincidences at high energies are now more densely packed, showing clear multiplicity measurement at these energies. Much of the scatter of coincidences between the two channels has been removed as a result of the smaller window size for acceptable coincidences. This proves that the plastic scintillator detector system has the ability to perform coincidence measurements with extremely small coincidence windows. To express this difference as it relates to the Helium-3 counters, both were modeled in MCNP.

4.3 MCNP Modeling Results

In MCNP, a source of ^{239}Pu was modeled in an environment where it was surrounded by four detectors. In one trial, these detectors were defined as the common Helium-3 filled detectors, while in the other trial the detectors were defined as the plastic scintillators used in this research. The goal of these models was to show the degree of quickness that the plastic scintillator detector system could implement over that of the Helium-3 detector system. The resulting measurement of single pulses for the Helium-3 detector system is shown in Figure 59, while the resulting measurement of single pulses for the plastic scintillator detector system is shown in Figure 60.

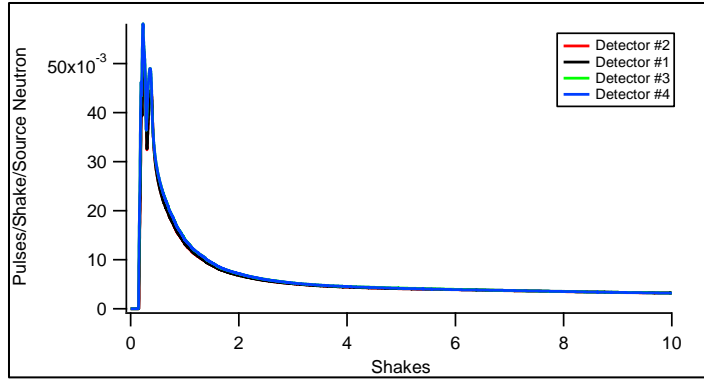


Figure 59 – Single Pulse Measurement of ^{239}Pu using Helium-3 Detectors

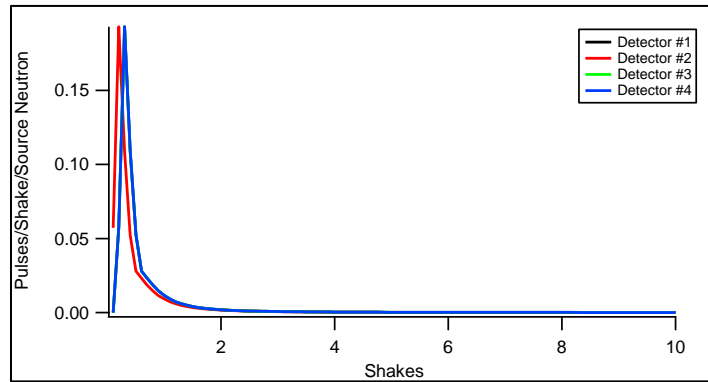


Figure 60 - Single Pulse Measurement of ^{239}Pu using Plastic Scintillator Detectors

From the results in Figures 59 and 60, the plastic scintillator detector is performing single pulse measurements much faster than that of the Helium-3 detectors, across all four detectors. Notice in the X-Axis that the unit is Shakes. Shakes are the MCNP unit of time, defined as $1 \text{ shake} = 10^{-8} \text{ seconds}$. In Figure 59, the Helium-3 detectors are still recording the single pulse measurement at the end of the time window, 10 shakes, never returning the initial starting point. Conversely, the plastic scintillators are quickly measuring the pulses on all four detectors and returning to the initial state within approximately 2.5 shakes of the initial pulse. This amounts to a pulse window time

of just 0.025 μs for the plastic scintillator detector system. To test this, coincidence measurements were modeled with the ^{239}Pu source, looking for double coincidences and triple coincidences across the possible combinations of detector pairings. The results are shown in Figures 61 and 62 for the plastic scintillator detectors. These are then compared to the results from the double and triple coincidence tests on the Helium-3 detector systems, shown in Figures 63 and 64, respectively.

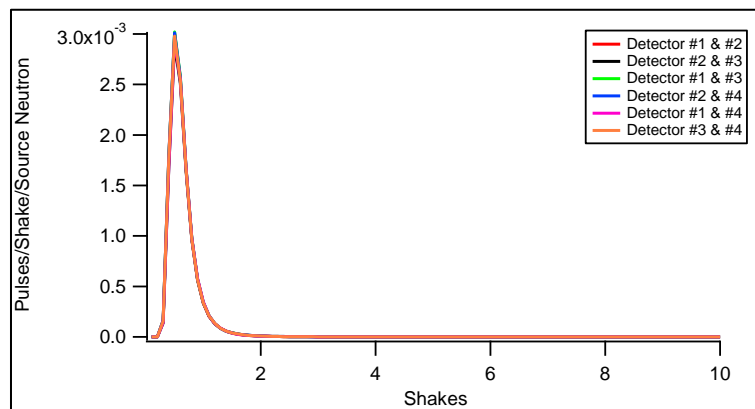


Figure 61 – Double Coincidence of ^{239}Pu using Plastic Scintillator Detectors

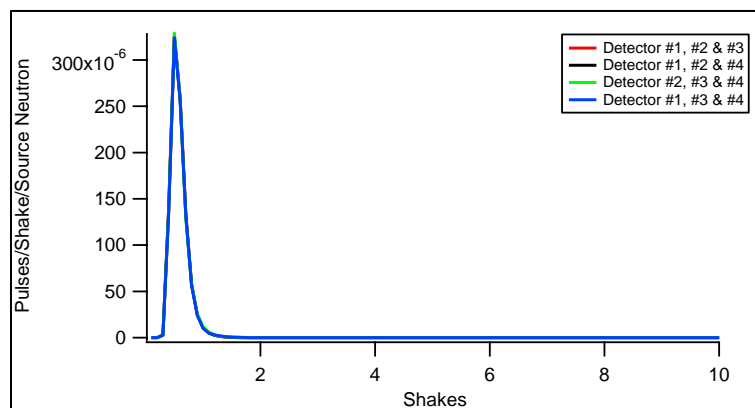


Figure 62 - Triple Coincidence of ^{239}Pu using Plastic Scintillator Detectors

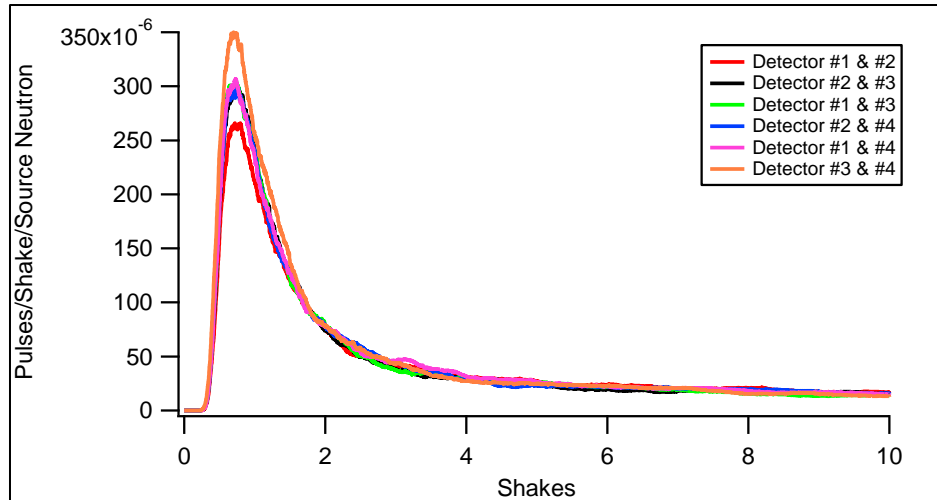


Figure 63 - Double Coincidence of ^{239}Pu using Helium-3 Detectors

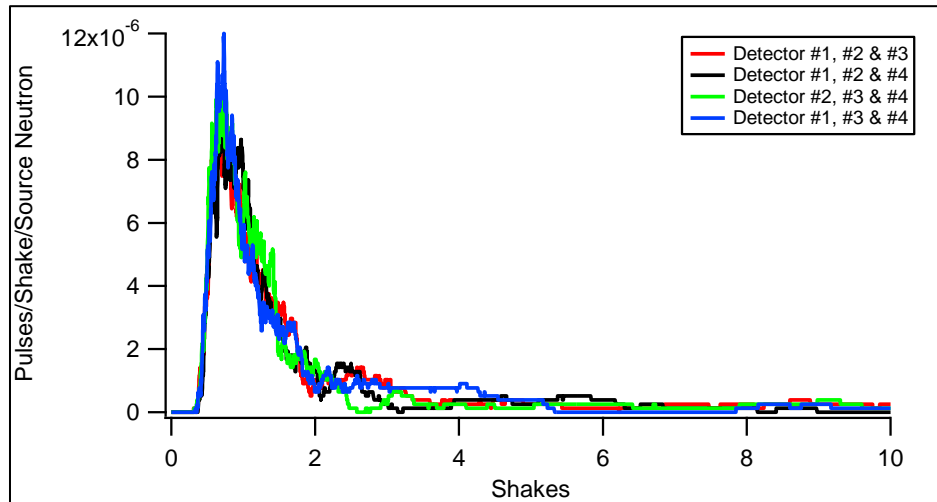


Figure 64 - Triple Coincidence of ^{239}Pu using Helium-3 Detectors

From these results, the theory that the plastic scintillators respond much faster to detections than that of the Helium-3 detectors, allowing for the establishment of a significantly smaller time coincidence window length, is confirmed. This smaller window increases the probability of “true coincidences” being seen by the detector system, which

is displayed in the comparison of Figure 62 and Figure 64. Notice that in Figure 62, the triple coincidences on all four possible pairings of the detectors resulted in near identical time coincidence measurements. However, with the results of the Helium-3 detectors (in Figure 64), there is a significant amount of noise in the measurements. These are the results of “false coincidences” being detected by the detector system due to the size of the time coincidence window. With the Helium-3 detectors, a coincidence window length of at least $0.1\ \mu\text{s}$ is required to adequately ensure coincidence, which only supports the findings displayed in Figure 64, not the results shown in Figures 59 and 63, which suggest a much longer coincidence length to ensure coincidence. However, with plastic scintillators, the time coincidence window can be drastically reduced.

Notice also, in Figures 61 and 62, that each detected coincidence pulse took approximately 1.5 shakes to measure. This leads to establishment of a coincidence window length of just 2 shakes, or $0.02\ \mu\text{s}$ for neutron time correlation measurements, which supports the use of the small time coincidence window in the double coincidence measurements of ^{60}Co in section 4.2. This time coincidence window can be set even lower for a pure gamma-gamma coincidence measurement, due to the pulse shape difference of photons versus that of neutrons. The MCNP results show the applicability of plastic scintillators in performing time-correlated measurements of neutron-neutron, neutron-gamma, and gamma-gamma multiplicity measurements, and how they compare to the Helium-3 detectors. As a result of these measurements, the plastic scintillator systems prove to be the superior system due their ability to utilize a significantly smaller time coincidence window, ensuring that only “true coincidences” are seen by the detector system.

CHAPTER 5

CONCLUSIONS AND FUTURE WORK

To conclude, the research shown in this thesis confirms that the use of plastic scintillators in the application of detecting neutrons can be a reliable alternative technology to the commonly used method of ^3He gaseous proportional counters.

The objectives of this thesis were as follows. First, design and construct a neutron detector using a plastic scintillator. Second, develop a technique for separating detected gamma rays from detected neutrons. Lastly, design an array of four scintillation detectors to study time coincidence measurements. These three objectives would allow the system to detect multiple neutrons from the same fission reaction using a single time scale for the four channels, and would lead to the possibility of performing fast neutron multiplicity measurements, thus helping to achieve the goals of non-proliferation.

In this work, a review of engineering fundamentals and literature review were performed to recognize the efforts of previous research projects. To achieve the thesis objectives, the array of fast neutron detectors was developed using novel plastic scintillation materials and digital data analysis electronics based on the field-programmable gate arrays. The plastic scintillator EJ-299-33A (Eljen Technologies) with the unique neutron / photon pulse shape discrimination properties was utilized as a fast-neutron detection material. The ten-stage photomultiplier tube was used as an optical readout device. The output signal of the photomultiplier's anode was directly digitized with the on-the-fly digital waveform processing and analysis. Because this scintillator is sensitive to gamma-rays, a technique was required that would adequately separate

neutron signals from gamma-ray signals. The pulse shape discrimination analysis technique based on the temporal differences of the detector signal's waveforms for each type of radiation was applied. For photons, the pulses produced by the scintillator material decayed faster than for neutrons. By taking advantage of these differences in pulse shapes, the data analysis system was showed to be capable of adequately separating neutron signals from photon signals employing the ratio of the partial integration time to the total integration time for each waveform. This technique was tested using a Plutonium-Beryllium neutron source that emits neutrons and photons simultaneously, and then confirmed using a source of Cobalt-60, which emits only photons.

In the experiments using the Plutonium-Beryllium source, the pulse shape discrimination technique resulted in the effective separation of photon and neutron signatures. Likewise, the test with the Cobalt-60 source proved the reliability of the technique by only detecting photons. This work was presented at the 2014 Annual American Nuclear Society Student Conference held at Pennsylvania State University [63].

Lastly, because a fission source with neutron multiplicity was not available on the UNLV's campus, the time correlation experiments were carried out using the source of Cobalt-60. These tests showed that the plastic scintillator detector system can perform gamma-gamma multiplicity measurements through the time coincidence analysis of gamma rays emitted from the Cobalt-60 source with the coincidence resolving time of approximately 0.02 μ s.

The computational modeling of neutron multiplicity measurements of a fission source of Plutonium-239 with a four-detector array was executed using the Monte Carlo N-Particle Transport code. The analysis of modeling data showed the significantly smaller coincidence resolving time for plastic scintillators compared to that of the Helium-3 detector systems, approximately 0.02 μs for the plastic scintillator versus about 1 μs for the Helium-3 counter.

Based on these results and the measured relationship of photon and neutron detector responses, it can be concluded that this detector system can perform not only gamma-gamma coincidence measurements, but also neutron-neutron (multiplicity) and neutron-gamma coincidence measurements with the coincidence resolving time much shorter than that of Helium-3 counters. The shorter gate interval enables limiting the probability of false coincidences being counted. These observations lead to determination that the fast neutron detection system based on the plastic scintillator is indeed a reliable alternative technology to the Helium-3 detectors commonly used in the nuclear industry.

However, the research does not stop there. To confirm the results of the time coincidence modeling of the four detector array, an experiment must be done using a fission source, so as to measure actual neutron multiplicities. This will then lead to the experimental confirmation of the neutron-neutron coincidence resolving time, which is expected to be just slightly longer than that of the gamma-gamma coincidence resolving time as it was measured through the use of the pulse shape discrimination. Likewise, this future research would allow the tests of the multi-detector array in neutron multiplicity measurements using fission events, which could not be done for this project due to the lack of a neutron multiplicity source available.

In addition, other future work includes the optimization of the detector system by using other technological components. One such example is the replacement of the photomultiplier tube with the solid state silicon photomultiplier (SiPM), a 2-in by 2-in panel with 64 pixels for the avalanche amplification of scintillation light pulses. This photomultiplier would also have to be used with an advanced version of the EJ-299-33A scintillating material, replacing the cylindrical design with that of a 2-in by 2-in cube design. Another example of component optimization is the conversion of the digital components to a smaller, more portable version. This component optimization ultimately leads to the development of a compact and portable detector design for in-the-field based applications. This work directly impacts the need of the industry for a reliable, advanced alternative to Helium-3 detectors for the application of ensuring that the nonproliferation goals of enhancing safety and security of nuclear fuel cycle and nuclear energy facilities are addressed.

APPENDICES

MCNP Input Code

```

Pu-239 Coincidence Measurements
C
1 3 -10.0 -1 imp:n=1
2 0 -114 117 imp:n=1
9 1 -1.08 -117 imp:n=1
12 like 2 but trcl=(0 10 0)
13 like 2 but trcl=(0 0 10)
14 like 2 but trcl=(0 10 10)
15 like 9 but trcl=(0 10 0)
16 like 9 but trcl=(0 0 10)
17 like 9 but trcl=(0 10 10)
10 0 114 #12 #13 #14 #15 #16 #17 -6 imp:n=1
11 0 6 imp:n=0

1 sph 0 0 0 1.0
114 rcc 0 -5 -5 20 0 0 2.55
117 rcc 0 -5 -5 5.08 0 0 2.54
6 sph 0 0 0 50

m1 1001.70c 0.0858621 6000.70c 0.9692905
m2 7014.70c 0.790 8016.70c 0.210 gas=1
m3 94239.70c 1.0
mode n
prdmp 2j 1 2
cut:n 2j 0 0
sdef par=n erg=D1 pos=0 0 0 WGT=5
SI1 L 0 5 10 14 20
SP1 0 1 1 1 1
f6:n 9 15 16 17
f8:n (9 15 16 17)
ft8 PHL 1 6 1
      1 6 2
      1 6 3
      1 6 4
e8 0 20 NT
fu8 0 20 NT
c8 0 20 NT
fs8 0 20 NT
t8 0 99i 10 NT
fq8 s c e t u
ctme 30
print

12 like 2 but *trcl=(0 0 0 0 90 90 90 90 0 90 180 90)
13 like 2 but *trcl=(0 0 0 0 90 90 90 180 180 90 270 180)
14 like 2 but *trcl=(0 0 0 0 90 90 90 270 180 90 360 270)
15 like 9 but *trcl=(0 0 0 0 90 90 90 90 0 90 180 90)
16 like 9 but *trcl=(0 0 0 0 90 90 90 180 180 90 270 180)
17 like 9 but *trcl=(0 0 0 0 90 90 90 270 180 90 360 270)

$Pu-239
$Detector Housing
$PS
$Repeat Housing
$Repeat Housing
$Repeat Housing
$Repeat PS
$Repeat PS
$Repeat PS

$Pu-239
$Detector Housing
$PS

$Plastic scintillator Material (density = 1.08 g/cc)
$Air
$Pu-239

$Source at center w/ energy distr 0-20MeV

$Detector #1
$Detector #2
$Detector #3
$Detector #4
$Time (Shakes)

$Repeat Detector Housing
$Repeat Detector Housing
$Repeat Detector Housing
$Repeat PS
$Repeat PS
$Repeat PS

```

REFERENCES

- [1] United States Department of Energy, Office of Nuclear Energy (2010). Nuclear Energy Research and Development Roadmap, Report to Congress. Retrieved from <http://energy.gov/ne/downloads/nuclear-energy-research-and-development-roadmap>
- [2] Moody, K. J., Hutcheon, I. D., & Grant, P. M. (2005). Nuclear Forensic Analysis. Boca Raton, Fla: CRC Press.
- [3] Shea, D. A., & Morgan, D. (2010). The Helium-3 Shortage: Supply, Demand, and Options for Congress (41419). Retrieved from Federation of American Scientists website: <http://http://www.fas.org/sgp/crs/misc/R41419.pdf>
- [4] Kouzes, R. T. (2009). The ^3He Supply Problem (18388). Retrieved from Pacific Northwest National Laboratory website: http://http://www.pnl.gov/main/publications/external/technical_reports/PNNL-18388.pdf
- [5] World Nuclear Association (2014, March). Outline History of Nuclear Energy. Retrieved February 2014, from <http://www.world-nuclear.org/info/Current-and-Future-Generation/Outline-History-of-NUclear-Energy/>
- [6] Tretkoff, American Physical Society, E. (n.d.). This Month in Physics History; May 1932; Chadwick Reports the Discovery of the Neutron. Retrieved February 2014, from <http://www.aps.org/publications/apsnews/200705/physicshistory.cfm>
- [7] Neutron Radiation Detector With Wand - BNC Gamma Spec. SAM 935 & 6894. (n.d.). Retrieved February 2014, from http://store.reuseum.com/Neutron_Radiation_Detector_With_Wand_BNC_Gamma_p/000011114020b14ls.htm
- [8] National Institute of Standards and Technology (n.d.). Fundamental Physical Constants. Retrieved February 2014, from <http://physics.nist.gov/cuu/Constants/index.html>
- [9] Coffey, J. (2010, February 17). Atom Diagram. Retrieved from <http://www.universetoday.com/56469/atom-diagram/>
- [10] Carron, N. J. (2007). An Introduction to the Passage of Energetic Particles through Matter. Boca Raton: CRC Press.

[11] Korean Atomic Energy Research Institute (n.d.). Table of Nuclides - U235. Retrieved February 2014, from <http://atom.kaeri.re.kr/ton/>

[12] Knoll, G. F. (2010). Radiation Detection and Measurement (4th ed.). Hoboken, N.J: John Wiley & Sons.

[13] Wagenaar, D. J. (1995, October 19). 7.1.3 The Bragg Curve. Retrieved from http://www.med.harvard.edu/jpnm/physics/nmltd/radprin/sect7/7.1/7_1.3.html

[14] Turner, J. E. (2007). Interactions of Heavy Charged Particles. In Atoms, Radiation, and Radiation Protection (3rd ed.). Weinheim: Wiley-VCH.

[15] Pianetta, P. (n.d.). Section 3-2 Electron Ranges in Matter. Retrieved from http://xdb.lbl.gov/Section3/Sec_3-2.html

[16] Krane, K. S., & Halliday, D. (1988). Introductory Nuclear Physics (3rd ed.). New York: John Wiley & Sons.

[17] Attix, F. H. (1986). Introduction to Radiological Physics and Radiation Dosimetry. New York: Wiley.

[18] Federation of American Scientists (1996). FM 8-9 Part I/Chptr 2 Conventional and Nuclear Weapons - Energy Production and Atomic Physics. Retrieved from <https://www.fas.org/nuke/guide/usa/doctrine/dod/fm8-9/1ch2.htm>

[19] Dictionary.com (n.d.). Fission. Retrieved March 2014, from <http://dictionary.reference.com/browse/fission>

[20] Wikipedia (n.d.). Nuclear fission.svg. Retrieved March 2014, from http://en.wikipedia.org/wiki/File:Nuclear_fission.svg

[21] Wikipedia (n.d.). ThermalFissionYield.svgdia. Retrieved March 2014, from <http://en.wikipedia.org/wiki/File:ThermalFissionYield.svg>

[22] Korean Atomic Energy Research Institute (n.d.). Table of Nuclides - He3. Retrieved March 2014, from <http://atom.kaeri.re.kr/ton/>

[23] Enqvist, A. E., Weinfurter, K. J., Flaska, M., & Pozzi, S. A. (2011). Characterization of a Mixed Multiplicity Counter Based on Liquid Organic Scintillators. IEEE Transactions on Nuclear Science, 58(5), 2413-2420.

[24] Royal Society of Chemistry (2012, January 12). Shortages Spur Race for Helium-3 Alternatives. Retrieved from

<http://www.rsc.org/chemistryworld/News/2012/January/helium-3-isotopes-shortage-alternatives-neutron-detectors.asp>

[25] Lintereur, A. T., Ely, J. H., Kouzes, R. T., Siciliano, E. R., Swinhoe, M. T., & Woodring, M. L. (2012). Alternatives to Helium-3 for Neutron Multiplicity Counters. IEEE Nuclear Science Symposium and Medical Imaging Conference Record, 3(4), 547-553.

[26] Persons, T. M., & Aloise, G. (2011). Technology Assessment: Neutron Detectors; Alternatives to Using Helium-3 (GAO-11-753). Retrieved from United States Government Accountability Office website: <http://http://www.gao.gov/assets/590/585514.pdf>

[27] Erickson, M. (2011). Boron-10 Neutron Detectors for Helium-3 Replacement (LA-UR 10-07751). Retrieved from Los Alamos National Laboratory website: http://http://www.lanl.gov/projects/feynman-center/_assets/pdf/boron-10-neutron-detectors-for-helium-3.pdf

[28] Simpson, A. P., Jones, S., Clapham, M. J., & McElhaney, S. A. (2011). A Review of Neutron Detection Technology Alternatives to Helium-3 for Safeguards Applications. INMM 52nd Annual Meeting.

[39] Stange, S., Karpus, P. J., Frame, K. C., Clay, W. A., Elmont, T. E., Esch, E. I., . . . Williams, R. B. (2006). Development of a Liquid Scintillator Neutron Multiplicity Counter (LSMC). IEEE Nuclear Science Symposium Conference Record, 12(4), 208-211.

[30] Patronis, N., Kokkoris, M., Giantsoudi, D., Perdikakis, G., Papadopoulos, C. T., & Vlastou, R. (2007). Aspects of GEANT4 Monte-Carlo calculations of the BC501A neutron detector. Nuclear Instruments and Methods in Physics Research A, 578, 351-355.

[31] Li, S., Xu, X., Cao, H., Yuan, G., Yang, Q., & Yin, Z. (2013). A real-time n/g digital pulse shape discriminator based on FPGA. Applied Radiation and Isotopes, 72, 30-34.

[32] Marocco, D., Belli, F., Esposito, B., Riva, M., Giacomelli, L., Reginatto, M., . . . Zimbal, A. (2009). High Count Rate Neutron Spectrometry With Liquid Scintillation Detectors. IEEE Transactions on Nuclear Science, 56(3), 1168-1173.

[33] Lee, P. S., Lee, C. S., & Lee, J. H. (2012). Development of FPGA-based Digital Signal Processing System for Radiation Spectroscopy. Radiation Measurements, 1-6.

- [34] Farsoni, A. T., Alemayehu, B., Alhawsawi, A., & Becker, E. M. (2013). Real-Time Pulse-Shape Discrimination and Beta-Gamma Coincidence Detection Infield-Programmable Gate Array. *Nuclear Instruments and Methods in Physics Research A*, 712, 75-82.
- [35] Bagi, J., Dechamp, L., Dransart, P., Dzbikowicz, Z., Dufour, J. L., Holzleitner, L., . . . Wilson, M. (2009). Neutron Coincidence Counting with Digital Signal Processing. *Nuclear Instruments and Methods in Physics Research A*, 608, 316-327.
- [36] Sulyaev, Y. S., Puryga, E. A., Khilchenko, A. D., Kvashnin, A. N., Polosatkin, S. V., Rovenskikh, A. F., . . . Grishnyaev, E. V. (2013). Multi-Purpose Fast Neutron Spectrum Analyzer With Real-Time Signal Processing. *Nuclear Instruments and Methods in Physics Research A*, 720, 23-25.
- [37] Stevanato, L., Cester, D., Nebbia, G., & Viesti, G. (2012). Neutron Detection in a High Gamma-Ray Background with EJ-301 and EJ-309 Liquid Scintillators. *Nuclear Instruments and Methods in Physics Research A*, 690, 96-101.
- [38] Bravar, U., Bruillard, P. J., Fluckiger, E. O., Macri, J. R., McConnell, M. L., Moser, M. R., . . . Woof, R. S. (2006). Design and Testing of a Position-Sensitive Plastic Scintillator Detector for Fast Neutron Imaging. *IEEE Transactions on Nuclear Science*, 53(6), 3894-3903.
- [49] Flaska, M., Enqvist, A., & Pozzi, S. A. (2009). Measurement of Fast Neutron/Gamma-Ray Cross- Correlation Functions with Cf-252 and Pu-Be Neutron Sources. *IEEE Nuclear Science Symposium Conference Record*, 13(243), 961-963.
- [40] Pozzi, S. A., Clarke, S. D., Flaska, M., & Peerani, P. (2009). Pulse Height Distributions of Neutrons and Gamma-Rays from Plutonium Oxide. *Nuclear Instruments and Methods in Physics Research A*.
- [41] Chichester, D. L., Pozzi, S. A., Dolan, J. L., Kinlaw, M. T., Kaplan, A. C., Flaska, M., . . . Watson, S. M. (2012). MPACT Fast Neutrons Multiplicity System Design Concepts (INL/EXT-12-27619). Idaho Falls, ID: Idaho National Laboratory.
- [42] Mattingly, J. (2012). Computation of Neutron Multiplicity Statistics Using Deterministic Transport. *IEEE Transactions on Nuclear Science*, 59(2), 314-322.

- [43] Ridnik, T., Dubi, C., Israelashvili, I., Bagi, J., & Huszti, J. (2014). LIST-Mode Applications for Neutron Multiplicity Counting. *Nuclear Instruments and Methods in Physics Research A*, 735, 53-59.
- [44] Mattingly, J. (2009). Polyethylene-Reflected Plutonium Metal Sphere: Subcritical Neutron and Gamma Measurements (Sand2009-5804/R2). Sandia National Laboratory.
- [45] Feynman, R. P., Hoffmann, F. D., & Serber, R. (1956). Dispersion of the Neutron Emission in U-235 Fission. *Journal of Nuclear Energy*, 3(1-2), 64-69.
- [46] Ensslin, N. (1998). Application Guide to Neutron Multiplicity Counting (LA-13422-M). Los Alamos, NM: Los Alamos National Laboratory.
- [47] Dierckx, R., & Hage, W. (1985). Neutron Signal Multiplet Analysis for the Mass Determination of Spontaneous Fission Isotopes. *Nuclear Science and Engineering*, 85(4), 325-338.
- [48] Hage, W., & Cifarelli, D. M. (1985). Correlation Analysis with Neutron Count Distributions in Randomly or Signal Triggered Time Intervals for Assay of Special Fissile Materials. *Nuclear Science and Engineering*, 89, 159-176.
- [49] Böhnel, K. (1985). The Effect of Multiplication on the Quantitative Determination of Spontaneously Fissioning Isotopes by Neutron Correlation Analysis. *Nuclear Science and Engineering*, 90, 75-82.
- [50] Cifarelli, D. M., & Hage, W. (1986). Models for a Three-Parameter Analysis of Neutron Signal Correlation Measurements for Fissile Material Assay. *Nuclear Instruments and Methods in Physics Research A*, 251(3), 550-563.
- [51] Miller, E. C., Clarke, S. D., Flaska, M., Pozzi, S. A., & Peerani, P. (2009). Development of a Post-Processing Methodology for Monte Carlo Multiplicity Analysis. *Transactions of the Institute of Nuclear Materials Management*, 12-16.
- [52] Estes, G. P., & Goulding, C. A. (1995). Subcritical Multiplication Determination Studies. *International Conference on Nuclear Criticality Safety*.
- [53] Estes, G. P., Goulding, C. A., Myers, W. L., & Hollas, C. L. (1999). Computational Analysis of HEU Subcritical Multiplication Experiments. *International Conference on Criticality Safety*, 2, 146-151.

- [54] Cifarelli, D., & Hage, W. (1986). Accelerator, Spectrometers, Detectors and Associated Equipment. Nuclear Instruments and Methods in Physics Research A.
- [55] Eljen Technologies (n.d.). EJ-299-33. Retrieved from <http://www.eljentechnology.com/index.php/products/plastic-scintillators/114-ej-299-33>
- [56] ADIT PMT (n.d.). B51B03 Photomultiplier Tube. Retrieved from <http://www.aditpmt.com/pmt-datasheets/B51B03W.pdf>
- [57] Bridgeport Instruments (n.d.). eMorpho - Multichannel Analyzer. Retrieved from <http://www.bridgeportinstruments.com/products/emorpho/emorpho.html>
- [58] WaveMetrics (n.d.). WaveMetrics - scientific graphing, data analysis, curve fitting & image processing software. Retrieved from <http://www.wavemetrics.com/>
- [59] Bridgeport Instruments (n.d.). qMorpho - 4-Channel MCA & DAQ. Retrieved from <http://www.bridgeportinstruments.com/products/qmorpho/qmorpho.html>
- [60] Wikipedia (2009, March). Cobalt-60m-decay. Retrieved April 1, 2014, from <http://en.wikipedia.org/wiki/File:Cobalt-60m-decay.svg>
- [61] Bridgeport Instruments (2009). eMorpho User's Manual Data Sheet. Austin, TX.
- [62] Lamarsh, J. R., & Baratta, A. J. (2001). Introduction to Nuclear Engineering (3rd ed.). Upper Saddle River, N.J: Prentice Hall.
- [63] Richardson, N. E., & Barzilov, A. (2014). *Neutron Measurements using EJ-299-33A Scintillator with Online Digital Pulse Shape Analysis*. Retrieved from American Nuclear Society - Pennsylvania State University website: <http://meetings.ans.org/student2014/>

VITA

Graduate College
University of Nevada, Las Vegas

Norman Richardson

Degree:

Bachelor of Science, Mechanical Engineering, 2012
University of Nevada, Las Vegas

Thesis Title: Time Correlated Measurements Using Plastic Scintillators with Neutron-Photon Pulse Shape Discrimination

Thesis Examination Committee:

Chairperson, Alexander Barzilov, Ph. D.
Committee Member, William Culbreth, Ph. D.
Committee Member, Yitung Chen, Ph. D.
Graduate Faculty Representative, Gary Cerefice, Ph. D.